# MICROSTRUCTURE MODELING IN WELD METAL

**S. A. David and S. S. Babu**

*Metals and Ceramic Division, Oak Ridge National Laboratory*

*Oak Ridge, TN 37831-6096, USA*



## ABSTRACT

Since microstructure development in the weld metal region is controlled by various physical processes, there is a need for integrated predictive models based on fundamental principles to describe and predict the effect of these physical processes. These integrated models should be based on various tools available for modeling microstructure development in a wide variety of alloy systems and welding processes. In this paper, the principles, methodology, and future directions of modeling thermochemical reactions in liquid, solidification, and solid state transformations are discussed with some examples for low–alloy steel, stainless steel, and Ni-base superalloy.

Thermochemical deoxidation reactions in liquid low–alloy steel lead to oxide inclusion formation. This inclusion formation has been modeled by combining principles of ladle metallurgy and overall transformation kinetics. The model's comparison with the experimental data and the ongoing work on coupling this inclusion model with the numerical models of heat transfer and fluid flow are discussed. Also, recent advances in theoretical and physical modeling of the solidification process are reviewed with regard to predicting the solidification modes, grain structure development, segregation effects, and nonequilibrium solidification in welds.

The effects of solid state phase transformations on microstructure development and various methods of modeling these transformations are reviewed. Successful models, based on diffusion–controlled growth and plate growth theories, on microstructure development in low–alloy steel and stainless steel weld metals are outlined. This paper also addresses the importance of advanced analytical techniques to understand the solid state transformation mechanisms in welds.

### DISCLAIMER

# INTRODUCTION

It has been recognized for many years that enormous opportunities and potential exist to develop a science-based tailoring of composition, structure, and properties of welds using an integrated modeling approach. There is a huge impetus to develop generalized and more reliable models that are based on fundamental principles for predicting microstructure development in both heat–affected zone (HAZ) and weld metal regions. However, microstructure development in the weld metal region is the most complicated.[1] This complication arises because of various physical processes that occur in the arc plasma vapor state,[2,3] weld metal liquid state,[4,5] and solid state.[6–9] The outcome of each physical process that dominates at higher temperature influences the phase changes at lower temperature. For example, physical processes such as elemental transport in the weld metal, evaporation of alloying elements from the weld metal, and gas–metal reactions control the final weld metal composition. The weld metal composition, in turn, controls the microstructure development during solidification and solid state transformations. This type of sequential dependency of microstructure development in weld metals exists in almost all alloy systems.

An example of this sequential dependency of microstructure development in low–alloy steel weld metal is illustrated in Fig. 1.[10] The steel weld pool region is usually heated to temperatures as high as 2500 K. As the weld metal cools from this temperature, (I) in the temperature range 2300 to 1800 K, the dissolved oxygen and deoxidizing elements in liquid steel react to form complex oxide inclusions of 0.1 to 1 μm size range; (II) in the temperature range 1800 to 1600 K, solidification of liquid to δ ferrite starts and envelops these oxide inclusions; later on (III) δ ferrite transforms to austenite; and (IV–VII) in the temperature range 1100 to 500 K, the austenite transforms to different ferrite morphologies such as allotriomorphic ferrite, Widmanstätten ferrite, and acicular ferrite. In this sequence of phase changes, the inclusion characteristics affect the solid state transformation of austenite to acicular ferrite.[7] The phase transformation from δ ferrite to austenite controls the austenite grain size which, in turn, controls the transformation kinetics of austenite to allotriomorphic ferrite.[11] Moreover, all of the processes shown from I–VII are controlled by weld metal composition. As mentioned earlier, the ultimate weld metal composition will be decided by the physical processes that occur in the arc plasma. This kind of sequential reaction is also quite common in other alloy systems. Therefore, it is practically impossible to model the microstructure development without considering the influence of all of the relevant physical processes.

Various sophisticated models using analytical and numerical approaches exist for describing the elemental evaporation and dissolution of gases,[3] heat transfer and fluid flow,[12] solidification,[4] and solid state transformation in welds.[7,8] However, an integrated model that comprises all of the above processes is yet to be developed. This integrated model must also be

capable of describing the microstructural degradation and changes during various postweld heat treatment schedules and service life. The development of such a model depends on the identification of various modeling tools for the fundamental description of various physical processes that occur in welds. This paper, in addition to reviewing tools available for microstructure modeling, describes work on (1) modeling inclusion formation in low–alloy steel welds, (2) modeling the solidification process, and (3) modeling the solid state transformations. These models are all part of an ongoing project to develop an integrated model for weld metal microstructure development.

## TOOLS FOR MICROSTRUCTURE MODELING

An overview of various analytical, experimental, and numerical tools that are used in various modeling activities is illustrated in Fig. 2. The modeling of weld metal microstructure needs to address the physical processes occurring at the macroscopic (heat transfer and fluid flow) scale and in the microscopic scale (grain nucleation and grain growth).[13] Since the complexity of each process is enormous, different approaches are used to model each one. Various models tend to solve the fundamental differential equations governing physical processes either by deterministic analytical techniques[14,15] or numerical methods like the finite element method (FEM) and finite difference method (FDM).[16-19] The physical processes are also simulated by probabilistic methods like Monte Carlo (MC) or cellular automata (CA) techniques.[13,20–23] In the models describing phase changes, thermodynamic descriptions of phases are needed. These data can be obtained from thermodynamic software such as MTDATA[24] and ThermoCalc™.[25] Several examples in which ThermoCalc™ software is used in conjunction with numerical and analytical methods to solve for solidification are available in the literature.[17,18,26]

In addition to the tools mentioned above, the experimental tools highlighted in Fig. 2 also play a vital role in validating the modeling activity and determining the underlying mechanisms of physical processes. For example, while modeling solid state transformations, many models assume local equilibrium at the interface. However, it is important to verify the validity of this assumption. This can be achieved by various experimental microanalytical tools like atom probe field ion microscopy (APFIM)[27–29] and analytical electron microscopy.[30,31] Tools like atomic force microscopy and thermomechanical simulators are used to validate various phase transformation mechanisms.[32,33] In addition, tools like differential thermal analysis (DTA) and differential scanning calorimetry (DSC) can be used to evaluate some key parameters like heat of fusion, stored strain energy, and transformation temperatures needed for modeling microstructure development in welds. A combination of the above tools is necessary for modeling microstructure development. In the following three sections, models for inclusion formation, solidification, and

solid state transformations in the welds, which use some of the above mentioned tools, are described.

## INCLUSION FORMATION

A reaction that is known to influence microstructure development is inclusion formation. In steel welds, inclusions are oxides and are the result of a deoxidation reaction. In low–alloy steel weld metal, inclusions can improve the toughness by promoting the formation of a high–toughness ferrite phase known as acicular ferrite. The acicular ferrite phase is in the form of thin lenticular plates of 1 to 2 μm length and 0.2 to 0.5 μm thickness and appears in an interlocking arrangement.[34–38] The maximization of acicular ferrite leads to an optimum combination of strength and toughness. A typical weld metal microstructure containing inclusions and acicular ferrite is shown in Fig. 3. The presence of oxide inclusions alone does not ensure the formation of acicular ferrite in steel welds. It is known that only certain kinds of inclusions aid in the nucleation of acicular ferrite;[7,34–36] the steel hardenability (chemical composition), austenite grain size, and welding conditions must also be conducive to form acicular ferrite in preference to other competing ferrite morphologies.[39–41] It is also known that an inadequate number density of inclusions leads to a reduced volume fraction of acicular ferrite.[39] Although certain inclusions aid in the formation of acicular ferrite, a very high volume fraction of inclusions may lead to poor properties. Therefore, it is necessary to control the inclusion characteristics to obtain the desired optimum microstructure.

The inclusion formation in a low–alloy steel weld is controlled by the concentrations of dissolved gases (such as oxygen and nitrogen) and deoxidizing elements (such as aluminum, titanium, silicon, and manganese). The dissolution of gases into the liquid steel is affected by the arc–atmosphere conditions around the molten steel. For example, it is known that the dissociation of diatomic gases into monatomic species affects the dissolution of gases into liquid steel.[42,43] The important inclusion characteristics are inclusion composition, size, and number density. The characteristics also include oxidation sequence and residual amounts of deoxidizing elements.[44–46] The residual amounts of deoxidizing elements in solid solution, such as Al, Ti, Si and Mn, that remain after the oxidation reaction control the transformation of austenite to ferrite at lower temperatures. Previous attempts[7,44,45] to predict inclusion composition assumed a fixed oxidation sequence of aluminum to $Al_2O_3$, titanium to $Ti_2O_3$, silicon to $SiO_2$, and manganese to MnO. This assumption was based on the ranking of the oxides $Al_2O_3$, $Ti_2O_3$ (or to other type of $Ti_xO_y$ oxides), $SiO_2$ and MnO as per their standard free energy of formation. However, the oxidation sequence may change as a function of concentrations of reacting elements. Moreover, previous

works did not model other inclusion parameters such as inclusion number density, size, and residual amounts of deoxidizing elements.

In this work, the inclusion formation is described for a given nominal concentration of dissolved gases and deoxidizing elements. Inclusion formation will also be controlled by the rate at which the weld cools. Therefore, in this work the inclusion formation is described as a function of weld metal composition and cooling conditions. The steps involved in this inclusion model include the calculation of (1) driving force for oxide formation, (2) homogeneous nucleation rates, (3) growth rates, and (4) overall oxidation kinetics as a function of temperature and composition. The methodologies for each of the above calculations are published elsewhere.[46] The isothermal oxidation kinetic calculations are then applied to the continuous cooling conditions.

Isothermal Overall Oxidation Kinetics

The overall isothermal oxidation kinetics at a particular temperature $T_1$ involving a deoxidizing element (M) and oxygen (O) dissolved in liquid steel to produce an oxide inclusion of $M_xO_y$ is given by the following equation:[46]

$$\zeta = 1 - \exp\left\{ - \left( (8\pi/15) I_V \left(\alpha_3^*\right)^3 t^{\frac{5}{2}} / \Omega \right) \right\}, \qquad (1)$$

where $\zeta$ is the extent of reaction, $I_v$ is the homogeneous nucleation rate of oxide $M_xO_y$ per unit volume per second, $\alpha_3^*$ is the parabolic thickening rate of oxides in liquid steel, $t$ is the time of reaction at temperature $T_1$, and $\Omega$ is the equilibrium volume fraction of $M_xO_y$ at $T_1$. The volume fraction is given by the following equation:

$$\Omega = \left(c_{\underline{M}}^{l} - c_{\underline{M}}^{il}\right) / \left(c_{\underline{M}}^{i} - c_{\underline{M}}^{il}\right) \qquad (2)$$

where $c_{\underline{M}}^{l}$ is the nominal concentration of the deoxidizing element, $c_{\underline{M}}^{il}$ is the concentration of deoxidizing element in the liquid in equilibrium with the inclusion, and $c_{\underline{M}}^{i}$ is the concentration of deoxidizing element in the inclusion. The equilibrium concentration of deoxidizing element, $c_{\underline{M}}^{il}$, is obtained by the construction of a tie line to the deoxidation phase diagram[46] (the concentrations are in mole fraction). In all the above calculations, multiphase equilibria between various oxides and

liquid steel are not considered. The expressions for calculating other terms $\alpha_3^*$ and $I_v$ are given elsewhere.[46] Equation (1) enables one to predict the isothermal oxidation kinetics for various oxides as a function of nominal composition and temperature.

Isothermal oxidation kinetic calculations were applied to two weld metal compositions (SW1: Fe-0.07C-0.8Si-1.7Mn-0.025Ti-0.026Al-0.084O wt % and SW2: Fe-0.07C-0.3Si-1.7Mn-0.003Ti-0.017Al-0.024O wt %), and the time–temperature–transformation diagrams for $\zeta = 0.1$ were calculated as a function of temperature. The comparisons are shown in Fig. 4. The difference in weld metal deposit chemistry changed the oxidation sequence as a function of decreasing temperature from 2300 K. In the SW1 weld, the reaction sequence is $Al_2O_3$, $MnO.Al_2O_3$, $Ti_3O_5$, $FeO.Al_2O_3$, $TiO_2$, $SiO_2$, and MnO. In the case of SW2, the reaction sequence is $Al_2O_3$, $MnO.Al_2O_3$, $FeO.Al_2O_3$, $Ti_3O_5$, $TiO_2$, $SiO_2$, and MnO. As SW2 contains less Ti than SW1, the $Ti_3O_5$ reaction is shifted below the $FeO.Al_2O_3$ reaction. Similarly, the MnO reaction is shifted to longer times in SW2, as oxygen content is lower than SW1. The plots show the sensitivity of TTT diagrams to weld composition. Thus, the present approach is capable of predicting the sequence of the oxidation reactions as a function of temperature and composition. However, this calculation method has to be modified to account for continuous cooling conditions in the weld and also changes in the weld metal composition as the oxidation reaction proceeds.

Continuous Cooling Oxidation Kinetics

Isothermal oxidation kinetics calculations were applied to continuous cooling conditions using the following steps: (1) the approximate cooling curve equation given by Ion et al.[47] is used for calculating the cooling rates in the weld metal; (2) kinetic calculations were carried out until the liquidus temperature, ~1800 K; (3) the reactions (i.e., sulfides and nitrides) that occur during solidification were not considered; (4) the extent of reaction obtained in Equation 1 was extended to continuous cooling by assuming the additivity of oxide volume fractions that form as a function of temperature during cooling; (5) as the extent of the reaction of an oxide reaches 0.9, the liquid composition was reset to account for the depletion of oxygen and deoxidizing element concentrations; (6) the integrated number density of the first forming oxide was taken as the final number density of inclusions in the steel weld (this assumption is based on the observation of heterogeneous and layered inclusion structures).[44] The calculation of final inclusion number density is given by:

$$Number\ Density = \sum_{i=T_{start}}^{i=T_{end}} I_V^{oxide1} \times \Delta t_i \qquad (3)$$

where $I_V^{oxide1}$ is the nucleation rate of the first forming oxide as a function of temperature, and $\Delta t_i$ is the time spent at each temperature from $T_{start}$, the temperature at which the first oxide starts to form, to $T_{end}$, the temperature at which the extent of reaction, $\zeta$, of the first oxide reaches 0.9. The accumulated volume fraction of oxide inclusions at the liquidus temperature was taken as the final volume fraction of oxides, and the residual liquid composition at 1800 K was related to the amount of deoxidizing elements in solid solution. With the knowledge of the final inclusion volume fraction ($V_f$) and final number density, the average inclusion radius was calculated ($V_f$ = Number Density $\times$ (4/3) $\times$ $\pi$ $\times$ $r^3$). The flow chart illustrating the calculation routine is shown in Fig. 5.

Inclusion Model Validation

The inclusion model developed in this work was validated with experimental results. The cooling rate data necessary for the calculation of inclusion characteristics were obtained by using the equation given by Ion et al.[47] However, it is important to note that these cooling rate calculations are approximate, and, ideally, one should use the weld metal cooling rate calculations which consider the heat flow and mass transfer in the weld pool region.[48] The calculations were validated with the experimental data of Kluken and Grong.[44,49] A comparison of experimental results of inclusion composition and final number density published by Kluken and Grong[44] with the calculations of the present inclusion model are shown in Fig. 6. The comparison shows that the present inclusion model predicts a trend similar to that of the experimental data. However, the predictions are not exact. For example, the calculated number density is always lower than that of the experimental data, and there are some inaccuracies in the calculated volume fraction of inclusions. Other comparisons are published elsewhere.[50] The present inclusion model can reasonably estimate the liquid composition at the end of the oxidation reaction during weld cooling at 1800 K. The comparison (see Fig. 7) of experimental measurement and theoretical estimation of aluminum in solid solution shows a fair correlation. However, excellent agreement is observed with the predicted titanium levels in solid solution. The inaccuracies of the inclusion model in predicting inclusion characteristics could be attributed to the following reasons:

1. Preliminary work[50] with the use of more sophisticated numerical calculations, considering fluid flow and heat transfer conditions, indicated that the cooling rates given by the equation in the reference 47 are lower than actually expected in the weld pool. Therefore, the agreement between calculations and experiments for the number density and size predictions are expected to improve with more accurate cooling rate values.
2. The present model does not consider the formation of other complex oxides like $MnO.SiO_2$ (Rhodonite) and $Al_2O_3.SiO_2$ (Andalusite) during liquid steel cooling.

3. The present inclusion model does not consider the reactions that occur during solidification, e.g., the MnS, TiN formation during the final stages of solidification and in the solid state.

Further work is in progress to remove the above limitations in the present inclusion model.[50] In addition to the oxides that form in the liquid state, precipitates like TiN, TiC, and other carbo-nitrides that form in solid state will be considered. This precipitation will be related to the amount of residual elements that is present after the oxidation reaction.

Future Directions

Although the new inclusion model is capable of describing the inclusion formation in steel welds, there are limitations in the present model as described above. To improve the cooling rate predictions in the liquid steel weld metal region, ongoing work focuses on coupling heat transfer and the fluid flow calculation method developed by Mundra et al.[51] The predicted values seem to be comparable to those of experimental data. Moreover, recent experimental work has shown that fluid flow in liquid steel plays a vital role in determining the ultimate inclusion number density.[52] Therefore, future work must use the particle tracking approach to track the inclusion coarsening in steel weld metal. This is schematically illustrated in Fig. 8.

## WELD SOLIDIFICATION

Weld solidification controls the size and shape of grains, segregation, and defects such as porosity and hot cracks.[5] Moreover, it also controls the inclusion distribution.[53] Although there are some similarities between ingot or casting solidification and weld–pool solidification, modeling of the solidification in the weld metal region is complicated by several factors: (1) dynamic nature of the welding process, (2) unknown weld pool shape, (3) epitaxial growth, and (4) variations in temperature gradient and growth rate within the weld–pool region. Further, depending on the welding process, the weld metal solidification rate may vary from $10^2$ to $10^3$°C $s^{-1}$ for the conventional welding process to $10^5$ to $10^7$°C $s^{-1}$ for high–energy beam processes. In this section, various attempts at modeling the weld solidification by extending the current knowledge of freezing of single crystals, castings, and ingots are described. In addition, recent work on extending rapid solidification theories to weld metal solidification is discussed.

Modeling of weld or ingot solidification is associated with nucleation and growth of solid phase from liquid. Generalized weld solidification models, in addition to describing nucleation and growth, must be capable of describing solute distribution, grain structure development, and rapid solidification effects.[1,4,54,55] A basic understanding of these concepts is necessary to develop an integrated model capable of describing solidification in a wide variety of welding process conditions and alloy systems.

Nucleation

In welds, solidification proceeds from the pre–existing solid substrate, and, hence, there is little or no nucleation barrier. In the case of autogeneous welding, solidification occurs spontaneously by epitaxial growth. In cases where filler metal is used, epitaxial growth may still occur. In addition to heterogeneous nucleation on the solid base material, inoculants have been successfully used to promote nucleation.[56] Moreover, in the past dynamic methods for promoting nucleation such as weld–pool stirring and arc oscillation have been used to refine the weld metal solidification structure.[5] This grain refinement is attributed to dislodging of dendrites from the solidification front. These dendrite debris can act as heterogeneous nucleation site for growth of solid from liquid. Although, the mechanisms of nucleation in weld metal are well understood, not much attention is given to modeling this phenomenon. Often, weld solidification models assume the epitaxial growth in their models, and for most of the cases, the assumption seems to be appropriate. However, to describe the effect of inoculants, arc oscillations, and weld–pool stirring, heat and mass transfer models[51,12] have to be coupled with either probabilistic models such as CA[21–23] or deterministic models using the fundamental equations of nucleation as described earlier.[46]

Growth

The development of microstructural features during growth of solid in the weld metal region is controlled by the shape of the solid/liquid interface. The nature and stability of the solid/liquid interface is mostly determined by the thermal and constitutional (composition) conditions that exist in the immediate vicinity of the interface. Depending on these conditions, interface growth may occur by planar growth, or cellular or dendritic growth. Theories for interface stability under conditions of equilibrium at the interface for normal solidification, or under extreme nonequilibrium conditions prevalent during rapid solidification, have been developed.[14,57] These theories can be extended to weld–pool solidification.

The parameters that determine the solidification microstructure in castings are growth rates ($R_S$), temperature gradient (G), undercooling ($\Delta T_u$), and alloy composition. It is well known that the temperature gradient and growth rate are important in the combined forms $GR_S$ (cooling rate) and $G/R_S$ since they influence the scale of the solidification substructure and the solidification morphology, respectively. In welding, where molten pool is translated through the material, both and G and $GR_S$ vary considerably across the weld pool region. Figure 9 shows schematically the influence of G and R on the microstructural variations within the weld metal. The figure shows the regions of planar to cellular transition (PCT) and cellular to equiaxed transition (CET). An

example of the transition from planar to cellular–type solidification microstructure is shown in Fig. 10.

The method of using $GR_S$ and $G/R_S$ relations to depict the solidification modes is proved to be simple and elegant. However, modeling of solidification morphology in a typical weld must consider other factors such as the fluid flow, the density of grains at the fusion line taking part in the epitaxial growth, the effect of base plate texture on the growth patterns in the weld metal region,[23,58] and the amount of total undercooling ($\Delta T$). Although the CA models[22] can be used for modeling the spatial morphology and transitions from cellular to equiaxed solidification in casting processes, much work needs to be done in improving the extension of this method to welds.[23] For example, these models have to account for the base plate texture and effect of segregation. Work has been done to understand the effect of base plate textures on the development of weld metal solidification structure by characterizing single–crystal welds,[5] which is discussed later in this paper. In future solidification morphology models, such as CA techniques,[22,23] either must consider solute diffusion or have to be coupled with the numerical models that consider the diffusion of partitioning alloying elements between solid and liquid phases.[17,59] The solute partitioning or solute redistribution is very sensitive to weld metal solidification conditions and needs further attention for precise description of solid/liquid interface growth conditions.

Solute distribution

Solute distribution during weld pool solidification is an important phenomenon resulting in segregation that can significantly affect weldability, microstructure, and properties. Various studies on extending different solidification models to describe solute distribution are summarized.[5] In describing the solute distribution under dendritic growth conditions, consideration should be given to redistribution at the dendrite tip and in the interdendritic regions. The solute distribution at the dendrite tip is determined, to a larger extent, by the dendrite tip undercooling, which is made up of four components: thermal undercooling, kinetic undercooling, constitutional undercooling, and undercooling due to tip curvature.[5]

In welding, the first two contributions can be ignored. However, since the microstructures are much finer in scale in welds than in castings, the contribution to the total tip undercooling due to the curvature effect is very significant.[5] The effect of increased undercooling at the dendrite tip would be to solidify at a composition closer to the overall composition and thus reduce the extent of microsegregation. Dendrite tip undercoolings in welds have been estimated by measuring dendrite core compositions in two different alloy systems, Al–Cu and Fe–Nb, after gas tungsten arc welding.[59] The estimated dendrite tip undercooling has been found to be significant. Considering the solute redistribution in the interdendritic regions, it may be sufficient to extend the

solidification model for microsegregation in castings to welds. In such cases, the weld solidification models can assume little or no diffusion in the solid while complete mixing of solutes in the liquid by convection can be assumed. This can be achieved by the Scheil equation[60] or modified Scheil equations that consider the diffusion[17,59] in the solid during welding.

Grain structure development

As mentioned earlier, growth often occurs by epitaxial growth from the partially melted grains in the base metal. Therefore, the weld metal grain structure is predominantly determined by the base metal grain structure and the welding conditions. In addition, crystallographic growth competitions will influence the grain structure development. It is well known that grain growth into the liquid region is favored along easy growth crystallographic directions, for example <100> in cubic metals. Conditions for growth are optimum when one of the easy growth directions coincides with the heat flow direction. Welding conditions and heat flow significantly influence the weld metal solidification grain structure, in that they determine the weld pool shape and the heat flow directions.

Since the solid/liquid interface is essentially perpendicular to the heat flow direction, the pool shape influences the optimum growth direction. In recent years, a three–dimensional (3–D) relationship between travel speed, solidification velocity, and dendrite growth velocity has been developed with work on growth crystallography and dendrite selection process in Fe–Ni–Cr single crystal welds.[61–63] The results of these calculations for two welds of two different orientations are shown in Fig. 11(*b*) and (*c*). The two angles, $\theta$ and $\phi$, are used to describe the solidification front orientation [see Fig. 11(*a*)]. and hence the weld pool shape. Using these diagrams, one can determine the range, in terms of $\theta$ and $\phi$, over which different dendrite growth directions are stable. These types of geometrical models can also be used to describe the 3–D reconstruction of the weld pool shape. Recent work has extended these types of geometrical dendrite growth models to bicrystal welds.[64] It is obvious that these geometrical models will be crucial for modeling the weld solidification in commercial Ni-base superalloy single crystals, and also for analyzing the effect of base plate texture on the weld pool solidification.

Rapid solidification effects

With the increased use of high–energy beam processes, such as electron and laser beams for welding, observations of nonequilibrium microstructures under rapid cooling conditions are becoming common. Such observations are well documented for austenitic stainless steel welds. [65–69] Figure 12 shows a fully austenitic stainless steel weld microstructure in a laser weld, which would normally contain a duplex austenite plus ferrite microstructure. This microstructure

is attributed to a change in the mode of freezing from primary ferrite to primary austenite during rapid solidification. Modeling of this kind of transition in rapid solidification is just evolving.

In rapid cooling conditions, a significant departure from local equilibrium at solid/liquid interface may occur. As a result, nonequilibrium structure and, in some cases, partitionless solidification can be observed. The magnitude of these departures is not fully understood and characterized. Another consequence of rapid solidification effect is that plane front solidification may become stable at extreme rapid growth rates as illustrated in Fig. 13(*a*).[5] An additional effect of rapid solidification is the change in the liquidus and solidus temperatures as illustrated in Fig. 13(*b*).[70] In summary, the integrated weld solidification models must describe the transition from classical solidification to rapid solidification in a generalized form.

## SOLID STATE TRANSFORMATIONS

In general, inclusion formation and solidification are part of the phase transformations that occur in any weld metal microstructure development. However, in some of the alloys, the solid state transformations that occur in the weld metal region control the final microstructure and properties, as seen in the case of low–alloy steel welds (see Fig. 1). Therefore, modeling solid state transformations in welds is important in developing generalized, integrated models for weld metal microstructure development. In this section, various models that deal with the solid state transformation and that describe the microstructural development are briefly summarized, and the need for further improvement in the models is highlighted. Some of the examples to describe the solid state phase transformations in welds are discussed. In addition, the need for integrated models that describe both the microstructure development during welding and also the microstructural changes during service[9,71] and heat treatments[72] is emphasized.

### Modeling solid state transformations

Much work exists on modeling the solid state phase transformation in the HAZs.[8] Recently, a lot of attention has been given to modeling the microstructure in weld metal regions.[7] In addition to phase transformations in solid state during weld thermal cycles, an integrated model for microstructure development should consider other solid state phase changes such as grain growth, coarsening, and solute redistribution. Most of the recent work has concentrated on describing the solid state phase transformations with fundamental theories of phase transformations.[7,8,73] Various solid state transformations that occur in welds during welding and in service can be grouped into four categories as follows: (1) phase changes involving diffusional processes such as precipitation or dissolution of second phase in the matrix; (2) solid state processes involving grain growth,[20,21,47,72] coarsening, and solute redistribution;[9,71] (3) phase changes involving

displacive transformations such as martensitic transformations; and (4) phase changes such as spinodal decomposition.[74] Moreover, it is important to note that some of the above phase changes may occur concurrently and interact with each other. Therefore, a prior knowledge of various phase transformations that occur in an alloy system is necessary before developing a model for weld metal microstructure development.

Most of the solid state phase changes that occur in welds can be grouped under the phase transformations controlled by the diffusional processes. Some examples of diffusional processes are austenite to allotriomorphic ferrite transformation in steel welds, dissolution of carbonitride precipitates in steel welds, and decomposition of primary ferrite into duplex austenite–ferrite microstructure in austenitic stainless steels. In principle, modeling of diffusion–controlled phase transformation involves describing the kinetics of phase change with nucleation[75] and the growth/dissolution of second phase in a matrix. The growth/dissolution of second phase in the matrix can be modeled with the assumption of local equilibrium at the second phase/matrix interface. Often, thermodynamic description of equilibrium at the growth interface is obtained from published thermodynamic data or from thermodynamic software like ThermoCalc™.[25] In some cases, the models describing diffusional phase changes must be coupled with models of other solid state changes, e.g., the grain growth can be controlled by the concurrent precipitation or dissolution of precipitates.[47]

Other solid state changes that occur in welds, which are driven by minimization interfacial energy, are grain growth and coarsening. Grain growth in welds is either modeled by analytical equations[47] or by MC simulations.[20,21] A specific advantage of MC simulations is the capability to describe the 3–D morphology of grains during the grain growth process.[76,77] Despite MC simulation's success in describing the grain morphology, until recently there were no proven methods for a one-to-one correlation between simulated measures of grain size and time with experimental measures. Recently, Radhakrishnan and Zacharia[76,77] addressed the above issue and suggested a general method of deriving a one-to-one correlation between experiments and simulation. They also applied this modified simulation technique to thermal pinning of grain growth near the fusion zone (FZ) in welds.[78] In addition to this probabilistic MC simulation approach, recently Grong[79] has suggested an internal state variable approach for modeling solid state transformations including grain growth in welds.

Displacive transformations occur in most of the steel welds, e.g., transformation of residual austenite to acicular ferrite, bainite, and martensite.[80] An approximate kinetic model for bainite formation is coupled with the cooling rates in welds to model the formation of local–brittle zones in welds.[81] However, improvements to kinetic models of bainite are being pursued by Bhadeshia and coworkers[80] for better description of the microstructure developments in certain high–strength low–alloy steel welds that exhibit predominant bainitic microstructure. It is also

noteworthy that the displacive transformation kinetics and transformation morphologies are quite sensitive to the presence of external or internal stresses on welds. Upon application of elastic stresses during transformation from austenite to acicular ferrite, a change in the morphology of acicular ferrite plates and transformation–induced plasticity were observed.[33] This observation has to be studied further and must be modeled in order to understand the interaction between microstructure and residual stresses development in welds.

Spinodal decomposition has been reported in duplex austenite-ferrite microstructures of thermally aged stainless steel welds.[74] In this case, the spinodal decomposition occurs in the ferrite phase on aging at 748 K, by which the ferrite decomposes into Cr– and Fe–rich regions. The initial composition of ferrite and the aging temperature control the kinetics and feasibility of the spinodal decomposition. In this case, it is desirable to couple thermodynamic software[25] with either numerical[17,18] or analytical models of weld metal microstructure development.

In summary, the first step for an integrated and generalized model for describing solid state transformation is the identification of key transformations and their mechanisms in a given alloy system that may control the microstructure development. The next step in the model involves the coupling of models for diffusional decomposition, grain growth, coarsening, displacive transformation, and spinodal decomposition based on the feasibility of each reaction. Finally, these coupled models have to be interfaced with models for weld thermal history. Some of the examples, which use the tools of microstructure modeling mentioned above, are presented to show the methodology described here.

Austenite grain structure development in low–alloy steels

It is known that the transformation of austenite to various ferrite morphologies in low–alloy steel weld metal is very sensitive to prior austenite grain size.[10,11,80] Hence, there is a need for models to predict the austenite grain size as a function of weld metal compositions and welding process variables. Svensson et al.[82] derived an empirical model between prior austenite grain size, weld metal composition and welding heat input from experimental data with concentration variations in carbon, silicon, and manganese only. Therefore, this model can not be extended to new weld metal composition with confidence.

A model for austenite grain size can be derived by understanding the austenite grain development in low–alloy steel welds. The austenite grain development during weld cooling is related to two solid state phase changes, i.e., (1) transformation of δ ferrite to austenite during cooling by nucleation and growth at δ ferrite grain boundaries and (2) austenite grain growth after the completion of the δ ferrite to austenite transformation during weld cooling. Recent work[10] has focused on relating the driving force for transformation of δ ferrite to austenite ($\Delta G^{\delta->\gamma}$) to the experimental austenite grain size measured by Evans.[83] Evans has measured the prior austenite

grain size as a function of weld metal composition for a constant welding heat input. The driving force for transformation of δ ferrite to austenite ($\Delta G^{\delta->\gamma}$) for the same compositions was calculated from ThermoCalc™ software.[25]

The austenite grain size is assumed to be inversely proportional to the nucleation rate of austenite at the δ ferrite grain boundary, where the nucleation rate is a function of $\Delta G^{\delta->\gamma}$ as shown below;

$$Grain\ Size = 1/(nucleation\ rate)^A, \quad (4)$$

where *A* is the constant exponent, and the nucleation rate is given by the expression:

$$nucleation\ rate = B + C\ exp\{-D/(\Delta G^{\delta->\gamma})^2\}, \quad (5)$$

where *B* and *C* are constants. The experimental austenite grain size (in the units of meters) and the calculated $\Delta G^{\delta->\gamma}$ (in the units of J mole$^{-1}$) are fitted to Eqs. (4) and (5). The fitted constants are obtained as follows: A = 0.48974; B = $1.356\times10^8$; C = $4.0869\times10^8$; and D = 3525.4. The correlation between the predicted and experimental data is shown as a function of $\Delta G^{\delta->\gamma}$ in Fig. 14. The figure also shows expected schematic variations of austenite grain size with heat input. This result shows that austenite grain size estimation for a constant heat input can be made with a knowledge of $\Delta G^{\delta->\gamma}$ from thermodynamic calculations and demonstrates the sensitivity of the austenite grain development to the driving force for transformation of δ ferrite to austenite. However, this simple calculation has to be modified to the continuous cooling conditions and to a change in the weld heat input. Further work is necessary in this area.

Analysis of residual element segregation in stainless steel welds

Type 308 stainless steel welds with the addition of 0.007 wt % boron showed improved creep properties.[28] Since boron additions may improve the properties by altering the microstructure, attempts were made to relate the microstructures that develop during welding.[28] The microstructural development during welding was found to be similar in welds with and without boron addition.[28] Therefore, it is important to study the boron redistribution between phases during weld metal cooling. As the weld solidification continues, the distribution of boron will be altered depending upon its partitioning behavior between liquid, austenite, and ferrite. The

equilibrium solidification and partitioning in boron containing weld were simulated using ThermoCalc™ software[25] and the Scheil method.[60] The calculations assume no diffusion in the solidifying phases. Since the solubility levels of boron in ferrite and austenite are small, as the solidification proceeds, the remaining liquid gets enriched in boron. The boron in the liquid may diffuse along the ferrite–austenite interface by grain boundary diffusion mechanism and may segregate to ferrite–austenite interfaces. According to thermodynamic calculations, the boron concentration at the ferrite–austenite interface is likely to be on the order of 1 at. % B. This prediction can be validated using APFIM.

APFIM analysis was performed on a boron-containing weld in the as–welded state. A field ion micrograph of an austenite–ferrite interface is shown in Fig. 15(*a*). The interface was decorated by a series of brightly imaging atoms indicative of solute segregation. An atom probe composition profile measured across an austenite–ferrite boundary is shown in Fig. 15(*b*). The composition profile shows the presence of boron at the austenite–ferrite interface. The maximum boron concentration at the interface was found to be ~ 2 at. % which compares well with thermodynamic calculations. This work shows thermodynamic calculations can help to model the residual element effects in welds. Further work has been done to model the boron segregation and its incorporation into the carbides during high–temperature aging.[84]

Ni-base superalloy weld microstructure development

Recently, it has been recognized that welding of Ni-base single crystal superalloy will play a vital role in repair welding of land–based gas turbine components. As a result, modeling and characterization of microstructure development in Ni-base superalloy welds has gained importance.[29] Babu et al.[29] studied the microstructure development in an electron beam welded PWA–1480 single–crystal superalloy. A low magnification transmission electron micrograph [see Fig. 16(*a*)] shows a boundary between two dendrite arms. Along the interdendritic regions, large $\gamma'$ precipitates interlaced by thin films of $\gamma$ phase were observed. The morphology of these large $\gamma'$ precipitates with penetrated $\gamma$ phase suggests that these $\gamma'$ precipitates formed during the final stages of solidification through eutectic reaction, $L \rightarrow \gamma + \gamma'$. Within the core of the dendrite, fine, cuboidal $L1_2$–ordered $\gamma'$ precipitates were observed. Electron diffraction confirmed the presence of $\gamma'$ precipitates within the $\gamma$ matrix. The size of these cuboidal $\gamma'$ precipitates varied from 0.05 to 0.5 μm, and their average volume fraction was found to be ~ 75%. However, the volume fraction of $\gamma'$ phase varied from region to region (60 to 85 %) within a single dendrite.

The above microstructural development can be explained with the help of a quasi-binary diagram of the Ni-Al-Cr alloy system, as shown in Fig. 16(*b*). With this phase diagram, one can follow various phase transformations that occur during cooling from the liquid state. To illustrate the microstructural development in the PWA-1480 alloy, the phase changes in the Ni–11.0 at. %

Al–11.5 at. % Cr alloy, as it solidifies from the liquid state, are discussed below. According to the equilibrium phase diagram, the solidification to $\gamma$ starts at ~ 1698 K and is completed at ~ 1685 K. Since the weld cooling conditions are far from equilibrium conditions, this may not be an actual representation of the weld solidification. Therefore, one has to apply Scheil[60] analysis which assumes local equilibrium at the liquid–$\gamma$ interface to model weld solidification. In this case, the solidus temperature will be lowered as a result of alloying element partitioning into the liquid. The liquid composition will follow the boundary between the liquid and (L + $\gamma$) phase fields as dictated by the tie lines.

The variations in the compositions of the $\gamma$ matrix and liquid phase during such a solidification in a Ni–11.0 at. % Al–11.5 at. % Cr alloy (assuming Scheil's model) were calculated using the ThermoCalc™ software.[25] These calculations assume that there is no back diffusion in the $\gamma$ phase. The calculations showed that the aluminum concentration at the core of the $\gamma$ dendrite (which forms at high temperature) is lower than that of the $\gamma$ dendrite boundaries (which form at a lower temperature). The calculations indicate that the solidus temperature is lowered by 50 K, i.e., to 1635 K. ThermoCalc™ calculations also suggested that the final liquid, due to solute enrichment, will undergo a eutectic reaction at ~ 1630 K as shown in Fig. 16(*b*). The observation [see Fig. 16(*a*)] of large $\gamma'$ precipitates interlaced with films of the $\gamma$ phase supports this mode of solidification for the weld. The variations in the volume fraction of $\gamma'$ phase can be attributed to weld solidification segregation.

However, this work[29] is not strictly valid, since Ti, Ta, W, and Co will modify the partitioning characteristics between the $\gamma$ and $\gamma'$ phases. Therefore, one has to use other calculation methods.[85] Further work is necessary to extend the thermodynamic calculations with consideration of other elements to predict the partitioning characteristics of $\gamma$ and $\gamma'$ phases during continuous cooling and thermal aging conditions. This work shows that by combining thermodynamic calculations and microstructural characterization, more accurate and precise models of solid state phase transformation in any alloy system can be developed.

## SUMMARY

This paper discusses a wide variety of theoretical, numerical, and physical modeling activities to describe various physical processes that occur in the weld metal region, and also tools available for microstructure modeling. An overview of all these models indicates that it is indeed possible to develop an integrated and generalized model for prediction of weld metal microstructure development, as a function of weld metal composition and welding process variable for any alloy system. The paper also explains the sequential dependency of each of the physical processes in the welding situation and the integrated models that are able to describe this. The importance of the

fundamental understanding of mechanisms of physical processes in welds and the validation of models with advanced experimental tools is also emphasized.

## ACKNOWLEDGMENTS

The authors thank Drs. S. Viswanathan and A. N. Gubbi for their helpful comments; Dr. K. Mundra and Prof. T. DebRoy of The Pennsylvania State University for collaborative work on heat transfer and fluid flow in welds; K. Spence for editing; and for manuscript preparation. Research is sponsored by the Division of Materials Sciences, U.S. Department of Energy, under contract DE–AC05–84OR21400 with Lockheed Martin Energy Systems, Inc.

## REFERENCES

1. T. DebRoy and S. A. David: *Rev. of Mod. Phys.*, 1995, **67**, 85–112.
2. J. Szekely: *Advances in Welding Science and Technology*, S. A. David, Ed. ASM, Materials Park, Ohio, 1986, 3–14.
3. T. DebRoy: *Mathematical Modeling of Weld Phenomena*, H. Cerjak and K. E. Easterling, Ed., The Institute of Materials, London, 1993, 24–38.
4. S. A. David and J. M. Vitek: *Mathematical Modeling of Weld Phenomena*, H. Cerjak and K. E. Easterling, Ed., The Institute of Materials, London, 1993, 41–59.
5. S. A. David and J. M. Vitek: *Int. Mater. Rev.*, 1989, **34**, 213–245.
6. D. L. Olson, S. Liu, and G. R. Edwards: *Mathematical Modeling of Weld Phenomena*, H. Cerjak and K. E. Easterling, Ed. The Institute of Materials, London, 1993, 89–108.
7. H. K. D. H. Bhadeshia and L.–E. Svensson: *Mathematical Modeling of Weld Phenomena*, H. Cerjak and K. E. Easterling, Ed., The Institute of Materials, London, 1993, 109–180.
8. K. E. Easterling: *Mathematical Modeling of Weld Phenomena*, H. Cerjak and K. E. Easterling, Ed., The Institute of Materials, London, 1993, 183–200.
9. B. Buchmayr: *Mathematical Modeling of Weld Phenomena*, H. Cerjak and K. E. Easterling, Ed., The Institute of Materials, London, 1993, 227–240.
10. S. S. Babu, S. A. David, J. M. Vitek and T. DebRoy: Proceedings of an International Symposium on *Phase Transformations During Thermal/Mechanical Processing of Steel*, August 20–23, 1995, Vancouver, Canada.
11. N. A. Fleck, Ø. Grong, G. R. Edwards, and D. K. Matlock, *Weld. J.*, 1986, **65**, 113s-121s.

12. T. Zacharia and S. A. David: *Mathematical Modeling of Weld Phenomena*, H. Cerjak and K. E. Easterling, Ed., The Institute of Materials, London, 1993, 3–23.
13. M. Rappaz and Ch.–A. Gandin, *Acta Metall. Mater.*, 1993, **41**, 345–360.
14. W. Kurz and D. J. Fisher: *Fundamentals of Solidification*, Trans Tech. Aedermannsdorf, Switzerland, 1989.
15. I. Andersen and Ø. Grong: *Modeling and Control of Joining Processes*, T. Zacharia Ed. American Welding Society, Miami, Fla.., 1994, 329–336.
16 T. Zacharia, A. H. Eraslan, D. K. Aidun, and S. A. David: *Metall. Trans.*, 1989, **20B**, 645-659.
17. T. Matsumiya, T. Koseki, W. Yamada, and Y. Ueshima: *Nippon Steel Technical Report*, 1993, **57**, 50–56.
18. J. M. Vitek, S. A. Vitek, and S. A. David: *Metall. Mater. Trans. A.*, 1995, **26A**, 2007–2025.
19. J. Ni and C. Beckermann: *Metall. Trans.*, 1991, **21B**, 349.
20. Y. Chen, B. Radhakrishnan and R. G. Thompson: *International Trends in Welding Science and Technology*, S. A. David and J. M. Vitek, Ed., ASM, Materials Park, Ohio, 1993, 259–263.
21. B. Radhakrishnan and T. Zacharia: *Modeling and Control of Joining Processes*, T. Zacharia Ed., American Welding Society, Miami, Fla., 1994, 298–305.
22. Ch.–A. Gandin, M. Rappaz, and R. Tintillier: *Metall. Trans.*, 1993, **24A**, 467–479.
23. W. B. Dress, T. Zacharia, and B. Radhakrishnan: *Modeling and Control of Joining Processes*, T. Zacharia Ed., American Welding Society, Miami, Fla., 1994, 321–328.
24. S. M. Hodson, Metallurgical and Thermochemical Databank, National Physical Laboratory, Teddington, Middlesex, United Kingdom, 1989.
25. B. Sundman, B. Jansson, and J.–O. Andersson: *Calphad,* 1985, **9**, 153-190.
26. Z–K. Liu: *Solid –> Solid Phase Transformations*, W. C. Johnson, J. M. Howe, D. E. Laughlin and W. A. Soffa, Ed., The Minerals, Metals & Materials Society, Warrendale, PA., 1994, 39–44.
27. M. K. Miller and G. D. W. Smith: *Atom Probe Microanalysis: Principles and Applications to Materials Problems*, Materials Research Society, Pittsburgh, Pa., 1989.
28. S. S. Babu, S. A. David, J. M. Vitek, and M. K. Miller: *Applied Surface Science*, 1995, **87/88**, 207–215.
29. S. S. Babu, S. A. David, and M. K. Miller: accepted for publication in *Appl. Surf. Sci.*, 1995.
30. S. A. David: *Weld. J.*, 1981, **60**, 63s–71s.

31. J. A. Brooks, M. I. Baskes, and F. A. Greulich: *Metall. Trans. A.*, 1991, **22A**, 915–926.
32. A. Vevecka, H. Ohtsuka, and H. K. D. H. Bhadeshià: *Mater. Sci. Technol.*, 1995, **11**, 109–111.
33. S. S. Babu and H. K. D. H. Bhadeshia: *Mater. Sci. and Eng.*, 1992, **A156**, 1–9.
34. Ø. Grong and D. K. Matlock: *Int. Met. Rev.*, 1986, **31**, 27-48.
35. D. J. Abson: *Welding Institute Report 69/1978*, The Welding Institute, Abington, United Kingdom, 1980, 1-11.
36. D. J. Abson: *Welding in the World*, 1989, **27**, 76-101.
37. Y. Ito and M. Nakanishi: *Sumitomo Search*, 1976, **15**, 42-62.
38. S. Liu, and D. L. Olson: *Weld. J.*, 1986, **65**, 139S-149S.
39. P. L. Harrison and R. A. Farrar: *J. Mater. Sci.*, 1981, **16**, 2218–2226.
40. J. R. Yang and H. K. D. H. Bhadeshia: *Advances in Welding Science and Technology*, S. A. David, Ed., ASM, Materials Park, Ohio, 1986, 209–213
41. S. S. Babu and H. K. D. H. Bhadeshia: *Mater. Sci. Technol.*, 1990, **6**, 1005-1020.
42. S. A. David, T. DebRoy, and J. M. Vitek: *MRS Bull.*, 1994, **XIX**, 29-35.
43. S. A. David and T. DebRoy: *Science*, 1994, **257**, 497-502.
44. A. Kluken and Ø. Grong: *Metall. Trans. A*, 1989, **20**, 1335–1349.
45. F–C. Liao and S. Liu: *Weld. J.*, 1992, **71**, 1992, 94s-103s.
46. S. S. Babu, S. A. David, J. M. Vitek, K. Mundra, and T. DebRoy: *Mater. Sci. Technol.*, 1995, **11**, 186-199.
47. J. C. Ion, K. E. Easterling, and M. F. Ashby: *Acta Metall.*, 1984, **32**, 1949-1962.
48. K. Mundra, T. DebRoy, S. S. Babu, and S. A. David: submitted for publication in *Weld. J.*, 1995.
49. A. Kluken: "Modeling of reaction sequence during deoxidation and solidification of steel weld metals," Ph.D. thesis, University of Trondheim, Norway, 1990.
50. S. S. Babu, S. A. David, J. M. Vitek, K. Mundra and T. DebRoy: *Trends in Welding Research*, June 5–8, 1995, Gatlinburg, Tennessee.
51. K. Mundra, T. DebRoy, S. S. Babu, and S. A. David: *Trends in Welding Research*, June 5–8, 1995, Gatlinburg, Tennessee.
52. S. S. Babu and S. A. David: Unpublished work, Oak Ridge National Laboratory, Oak Ridge, Tennessee, 1995.
53. A. A. B. Sugden and H. K. D. H. Bhadeshia: *Metall. Trans. A*, 1988, **19A**, 669–674.
54. S. A. David, J. M. Vitek, T. Zacharia, and T. DebRoy: Proceedings of *Physical Aspects of Arc Welding*, September 1, 1993, IIW, Glasgow, United Kingdom, 95–112.

55. S. A. David, J. M. Vitek, S. S. Babu, and T. DebRoy: Proceedings of *42nd National Welding Conference*, Australia, Vol. 2., Welding Technology Institute of Australia, Silverwater, New South Wales, Australia, 1994.
56. J. C. Villafuerte, H. W. Kerr, and S. A. David: *Mater. Sci. and Eng.*, 1995, **A194**, 187–191.
57. M. C. Flemings: *Solidification Processing*, McGraw-Hill, New York, 1974.
58. S. S. Babu, H. K. D. H. Bhadeshia, L.–E. Svensson: *J. Mater. Sci. Lett.*, **10**, 1991, 142-144.
59. J. A. Brooks and M. I. Baskes: *Advances in Welding Science and Technology*, S. A. David, Ed., ASM, Materials Park, Ohio, 1986, 93–99.
60. E. Scheil: *Z. Metall.*, 1942, **34**, 70.
61. M. Rappaz, S. A. David, J. M. Vitek, and L. A. Boatner: *Metall. Trans, A.*, 1989, **20A**, 1125–1138.
62. M. Rappaz, S. A. David, J. M. Vitek, and L. A. Boatner: *Metall. Trans. A.*, 1990, **21A**, 1767–1782.
63. S. A. David, J. M. Vitek, M. Rappaz, and L. A. Boatner: *Metall. Trans, A.*, 1990, **21A**, 1753–1766.
64. M. Rappaz, S. A. David, J. M. Vitek, and L. A. Boatner: *Metall. Trans, A.*, 1993, **24A**, 1433–1446.
65. S. A. David and J. M. Vitek: *Lasers in Metallurgy*, K. Mukerjee and J. Mazumder, Ed., Warrendale, Pa., 1981, 2247–2254.
66. J. M. Vitek, A. DasGupta, and S. A. David, *Metall. Trans.*, 1983, **14A**, 1833-1841.
67. S. A. David, J. M. Vitek, and T. L. Hebble, *Weld. J.*, 1987, **66**, 289s.
68. S. Katayama and A. Matsunawa, *Proc. ICALEO*, 1984, 60–67.
69. J. W. Elmer, S. M. Allen, and T. W. Eagar, *Metall. Trans. A,* 1989, **20A**, 2117–2131
70. W. Kurz: *Fourth International Conference on Trends in Welding Research*, June 5–8, 1995, Gatlinburg, Tennessee.
71. J. M. Race and H. K. D. H. Bhadeshia: *International Trends in Welding Science and Technology*, S. A. David and J. M. Vitek, Ed., ASM, Materials Park, Ohio, 1993, 315–319.
72. R. C. Reed, Ph.D. Thesis, University of Cambridge, United Kingdom, 1990.
73. H. K. D. H. Bhadeshia, L.–E. Svensson, and B. Gretoft: *Acta Metall.*, 1985, **33**, 1271–1283.
74. J. M. Vitek, S. A. David, D. J. Alexander, J. R. Keiser, and R. K. Nanstad: *Acta Metall. Mater.*, 1991, **39**, 503–516.

75. J. W. Christian: *The Theory of Transformations in Metals and Alloys - Part I Equilibrium and General Kinetic Theory*, 2nd Ed., Pergamon Press, New York, 1981.

76. B. Radhakrishnan and T. Zacharia: *Metall. Mater. Trans. A,* 1995, **26A**, 167–180.

77. B. Radhakrishnan and T. Zacharia: *Metall. Mater. Trans. A,* 1995, **26A**, 2123–2130.

78 P. J. Alberry, B. Chew, and W. K. C. Jones: *Met. Technol.,* 1977, **4**, 317–325.

79. Ø. Grong: *Fourth International Conference on Trends in Welding Research*, June 5–8, 1995, Gatlinburg, Tennessee.

80. H. K. D. H. Bhadeshia: *Bainite In Steels*, Institute of Materials, London, 1992.

81. S. Suzuki, G. I. Rees and H. K. D. H. Bhadeshia: *Modeling and Control of Joining Processes*, T. Zacharia Ed., American Welding Society, Miami, Fla., 1994, 186–193.

82. L.–E. Svensson, B. Gretoft, and H. K. D. H. Bhadeshia: *Scand. J. Metall.,* 1986, **15**, 97–103.

83. G. M. Evans: *Weld. J.,* 1983, **62**, 313s-320s.

84. S. S. Babu, S. A. David, J. M. Vitek, and M. K. Miller: *Metall. Mater. Trans. A,* 1995, in press.

85. M. Enomoto, H. Harada, and M. Yamazaki, *Calphad*, 1991, **15**, 143.

# FIGURE CAPTIONS

Fig. 1 Schematic diagram of continuous cooling transformation showing the development of weld metal microstructure in low–alloy steels: (I) inclusion formation, (II) solidification of liquid to δ ferrite, (III) fully austenitic structure, (IV) nucleation of allotriomorphic ferrite, (V) growth of allotriomorphic ferrite all along the austenite grain boundaries, (VI) Widmanstätten ferrite formation, and (VII) acicular ferrite formation.

Fig. 2 An overview of theoretical, numerical, and experimental tools available for weld microstructure modeling.

Fig. 3 Typical weld metal microstructure observed in a low-alloy steel weld.

Fig. 4 A comparison of the transformation time (for fraction transformed, $\zeta = 0.1$) for various oxides as a function of temperature for two steel compositions: (*a*) SW1: Fe-0.07C-0.8Si-1.7Mn-0.025Ti-0.026Al-0.084O wt. % and (*b*) SW2: Fe-0.07C-0.3Si-1.7Mn-0.003Ti-0.017Al-0.024O wt. %.

Fig. 5 Flow chart illustrating the application of isothermal oxidation kinetic calculation to continuous cooling conditions. The calculation starts with a nominal weld composition at 2300 K. The cooling curves are then divided into small isothermal steps. The kinetic calculations are performed at each temperature and time interval and additivity of oxide volume fraction is assumed.

Fig. 6 Comparison of experimental inclusion characteristics measured by Kluken and Grong[44] and the calculated inclusion characteristics by the present inclusion model: (*a*) inclusion composition and (*b*) inclusion number density.

Fig. 7 Comparison of experimental aluminum and titanium in solid solution measured by Kluken and Grong[44] and the calculated estimates by the inclusion model.

Fig. 8 Schematic illustration of particle tracking approach to model the inclusion movement through the liquid weld pool using numerical heat transfer and fluid flow calculations.

Fig. 9 (*a*) Schematic illustration of weld microstructure across the fusion zone and (*b*) corresponding schematic variation of G, R, GR and G/R values as a function of position.

Fig. 10 Optical micrograph of stainless steel weld metal region and heat affected zone. The micrograph clearly shows the fusion line, with planar growth; region of transition from planar to cellular growth; and the region of cellular growth.

Fig. 11 (*a*) Schematic diagram of the weld pool showing the orientation of the fixed set of reference axes, *x*–*y*–*z*, and the angles $\psi$, $\phi$, and $\theta$ (the *z*–axis of this reference frame is perpendicular to the top surface of the bicrystal, and the *x*–axis coincides with the welding direction); (*b*) velocity isopleth map of the minimum dendrite tip velocity $|V_{hkl}|$, normalized to the beam velocity $|V_b|$, as a function of the orientation angles $\theta$ and $\phi$ of the solidification front normal $n$ for a weld in the [100] direction on (001) face of the crystal; and (*c*) for a weld in the [111] direction on $(1\bar{1}0)$ face of the crystal.

Fig. 12 Duplex (austenitic plus ferrite) structure in conventional weld overlay and fully austenitic structure obtained by autogeneous laser weld on the same overlay.

Fig. 13 (*a*) Effect of velocity–dependent partition coefficient on dependence of dendrite tip radius on growth velocity and (*b*) variation of nonequilibrium solidus and liquidus temperatures and partition coefficient as a function of growth velocity.[70]

Fig. 14 The variation of austenite grain size (measured in welds deposited with a heat input of 1 kJ $mm^{-1}$) with driving force for transformation of δ ferrite to austenite ($\Delta G^{\delta->\gamma}$). The dark line is the fitted line with a relation given by Eqs. (4) and (5). Experimental data (open circles) are from ref. 83. The curves for 3 and 5 kJ $mm^{-1}$ are drawn schematically to illustrate the expected variation.

Fig. 15 (*a*) Field ion micrograph of the as-welded sample showing (δ) ferrite–austenite boundary and (*b*) composition profile indicating the presence of boron along the (δ) ferrite–austenite boundary.

Fig. 16 (*a*) Transmission electron micrograph of the PWA-1480 weld metal region in the as-welded condition showing two dendritic grains, dendritic boundary, and eutectic γ′ precipitate (marked by an arrow) along the dendritic boundary. The electron diffraction pattern (inset), taken near to the $[001]_\gamma$ zone, shows the superlattice reflections from γ′ precipitates. (*b*) A quasi-binary diagram of the Ni-Al-Cr system with 11.5 at. % Cr calculated by ThermoCalc™ software.[25] The dotted line shows the composition corresponding to 11.0 at. % Al. In this phase diagram, the tie lines are not in the plane of the diagram.

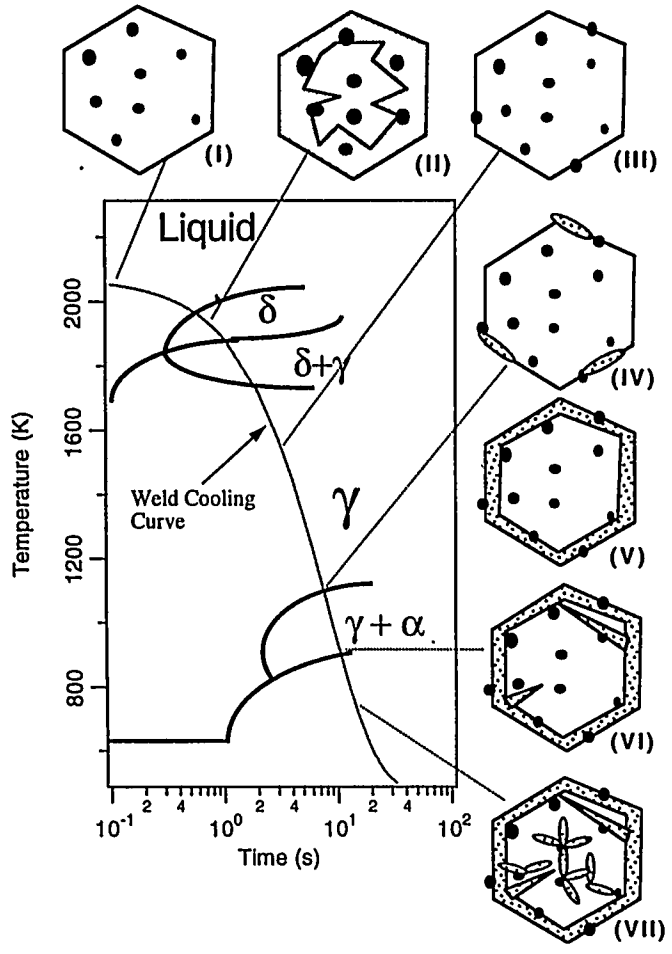


Fig. 1 Schematic diagram of continuous cooling transformation showing the development of weld metal microstructure in low–alloy steels: (I) inclusion formation, (II) solidification of liquid to δ ferrite, (III) fully austenitic structure, (IV) nucleation of allotriomorphic ferrite, (V) growth of allotriomorphic ferrite all along the austenite grain boundaries, (VI) Widmanstätten ferrite formation, and (VII) acicular ferrite formation.

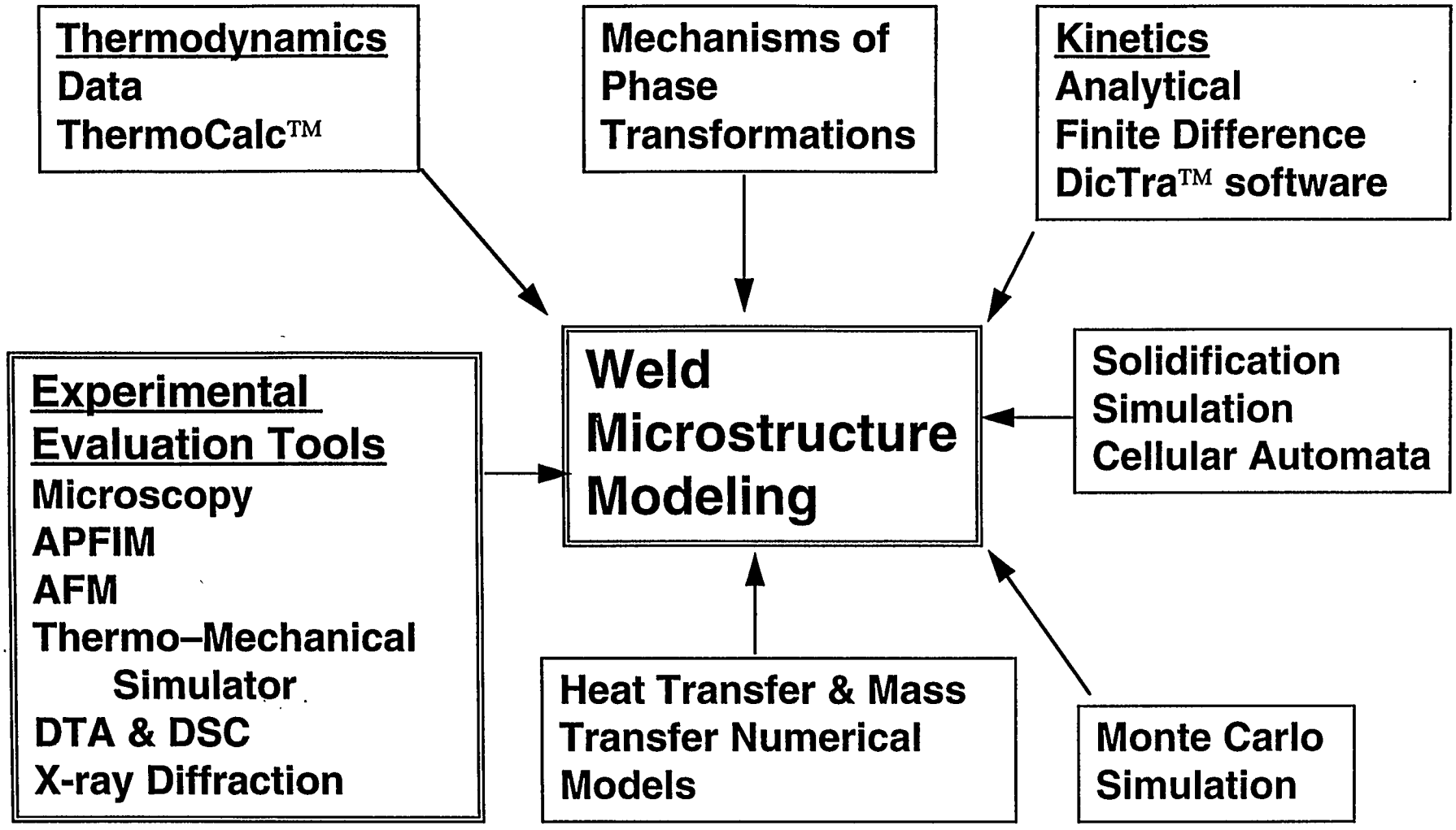


Fig. 2 An overview of theoretical, numerical and experimental tools available for weld microstructure modeling.

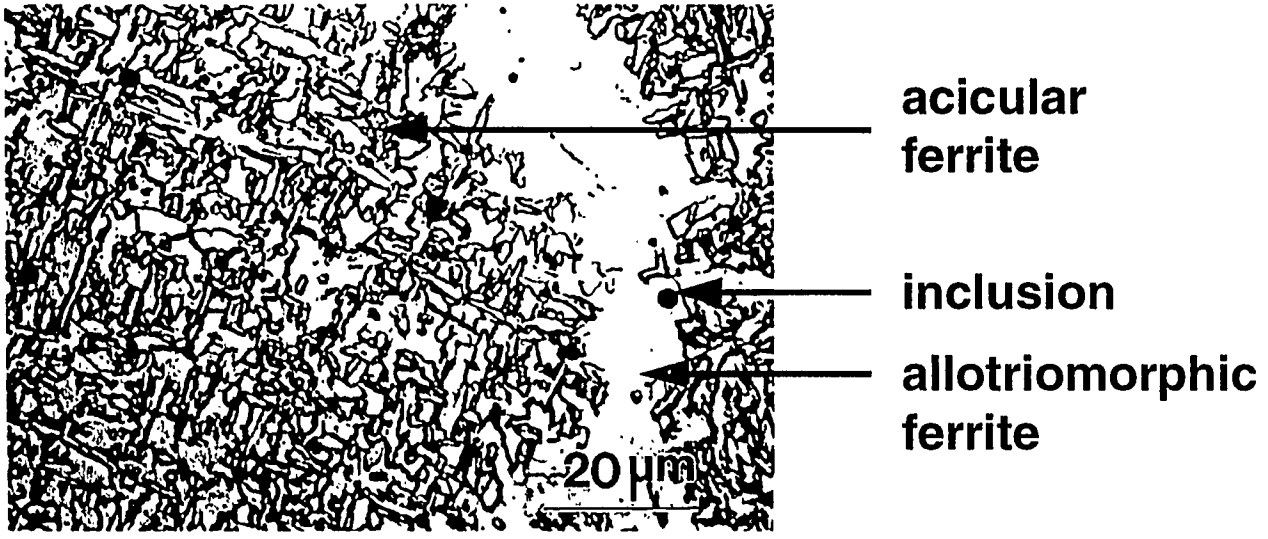


**Fig. 3 Typical weld metal microstructure observed in a low–alloy–steel weld.**

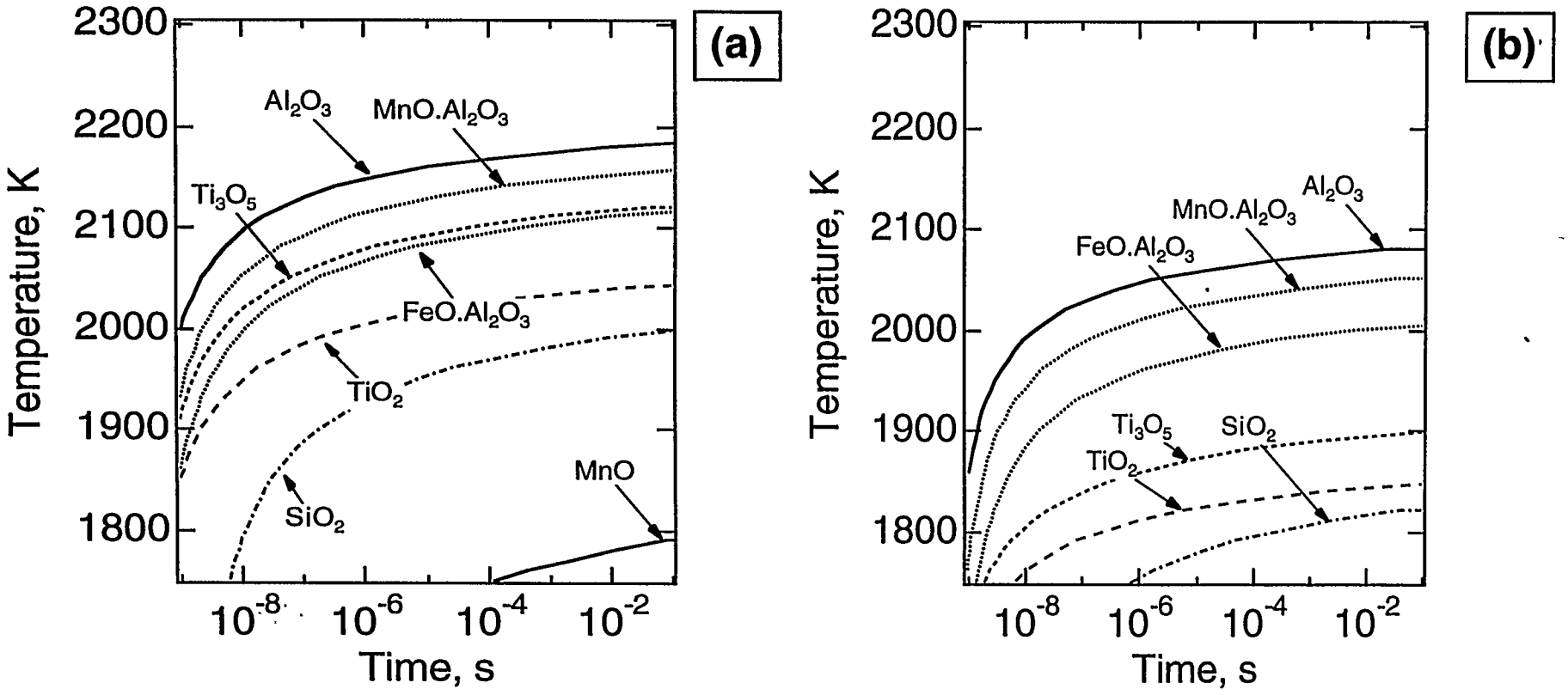


Fig. 4 A comparison of the transformation time (for fraction transformed, $\zeta = 0.1$) for various oxides as a function of temperature for two steel compositions: (*a*) SW1: Fe-0.07C-0.8Si-1.7Mn-0.025Ti-0.026Al-0.084O wt. % and (*b*) SW2: Fe-0.07C-0.3Si-1.7Mn-0.003Ti-0.017Al-0.024O wt. %.

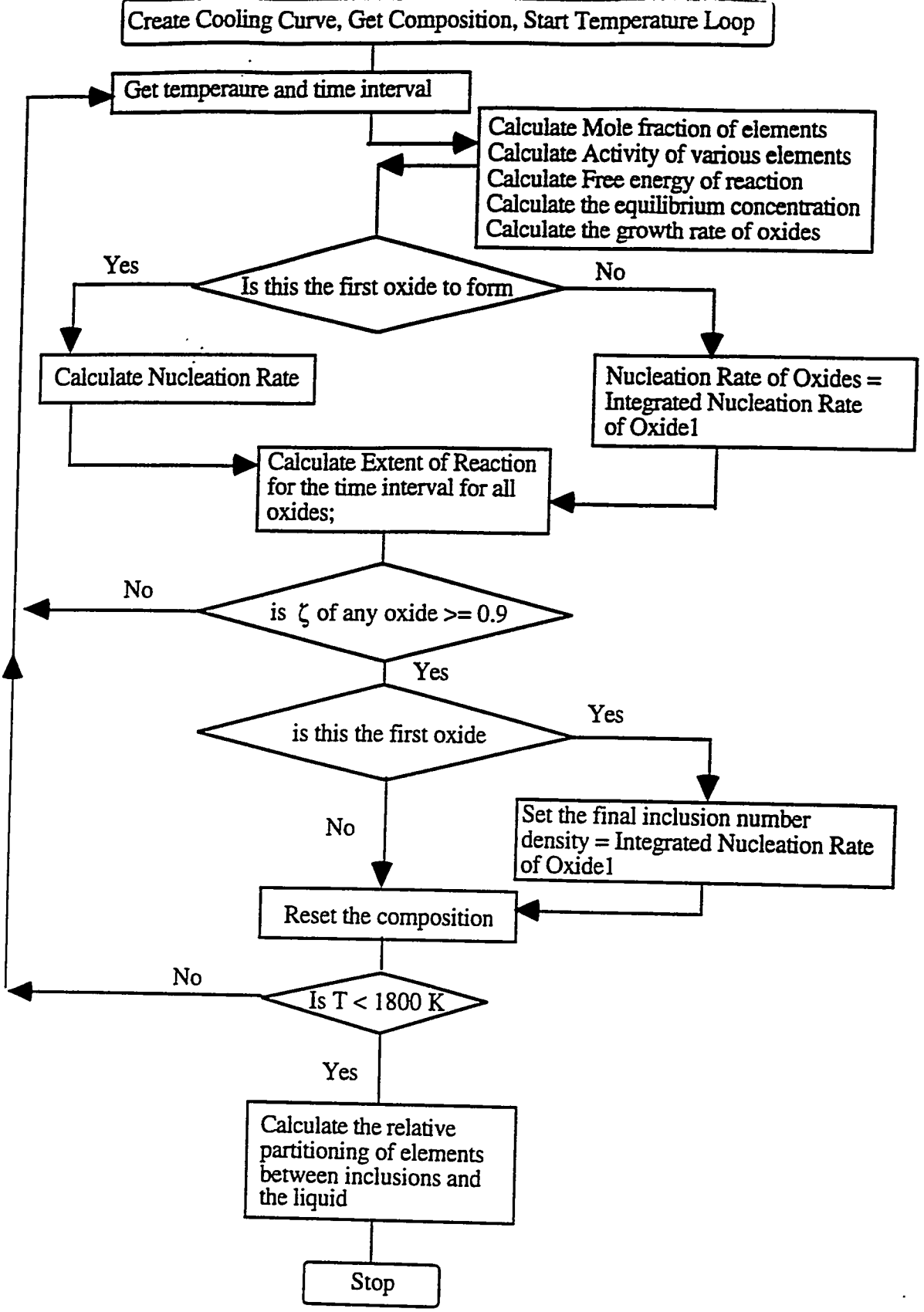


Fig. 5 The flow chart illustrating the application of isothermal oxidation kinetic calculation to continuous cooling conditions. The calculation starts with a nominal weld composition at 2300 K. The cooling curves are then divided into small isothermal steps. The kinetic calculations are performed at each temperature and time interval and additivity of oxide volume fraction is assumed.

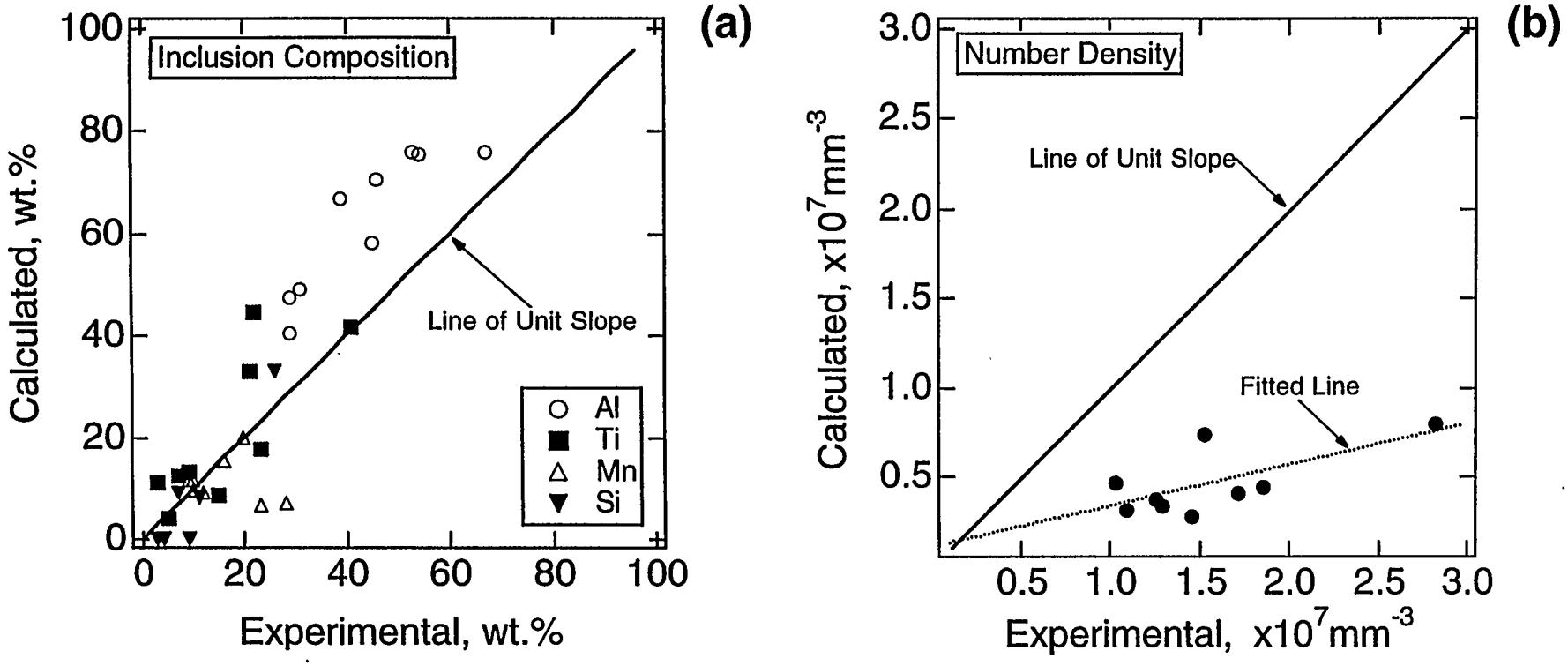


Fig. 6 Comparison of experimental inclusion characteristics measured by Kluken and Grong[44] and the calculated inclusion characteristics by the present inclusion model: (*a*) inclusion composition and (*b*) inclusion number density.

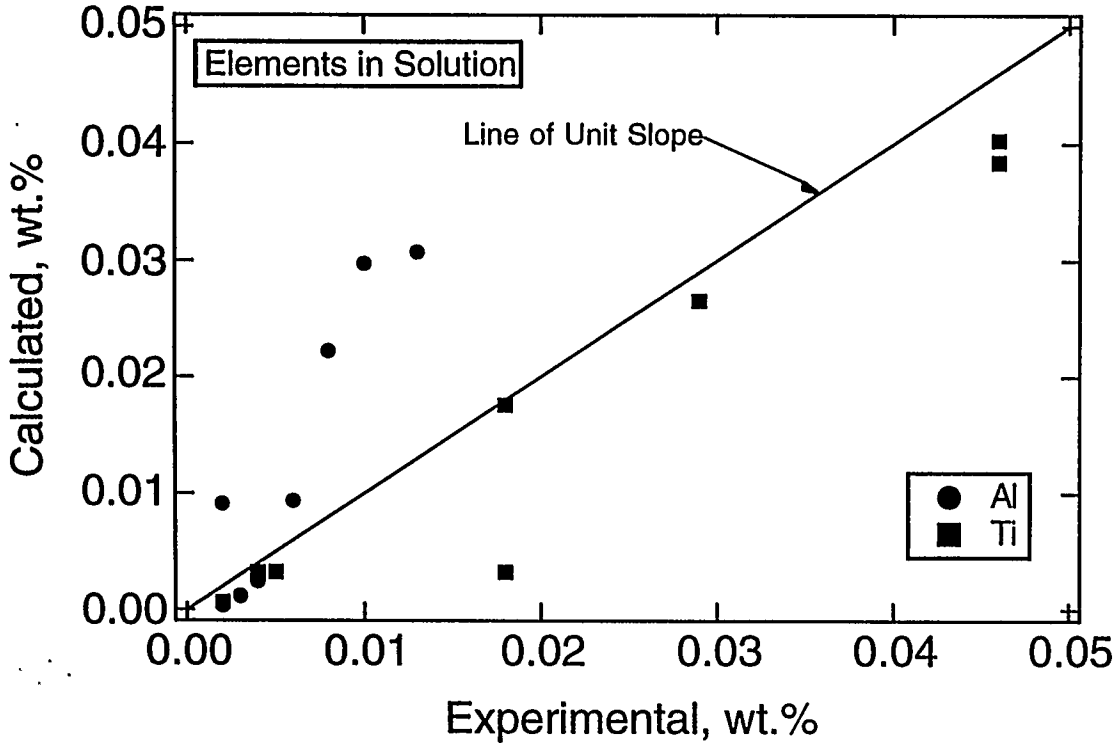


Fig. 7 Comparison of experimental aluminum and titanium in solid solution measured by Kluken and Grong[44] and the calculated estimates by the inclusion model.

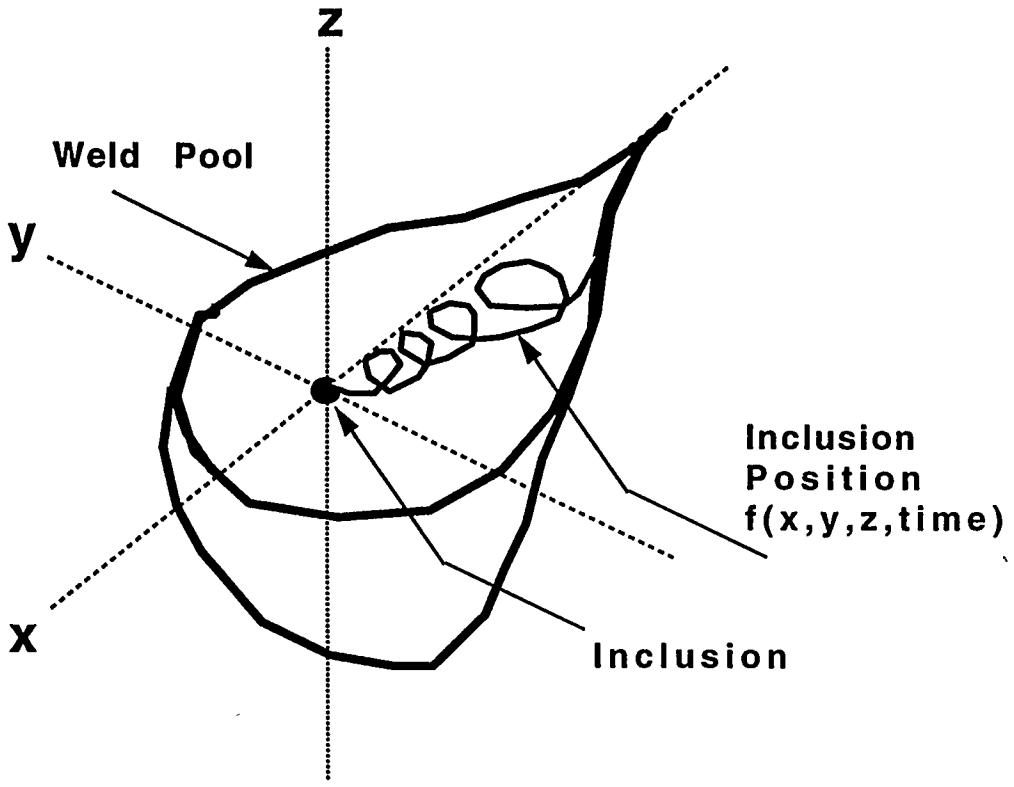


**Fig. 8 Schematic illustration of particle tracking approach to model the inclusion movement through the liquid weld pool using numerical heat transfer and fluid flow calculations.**

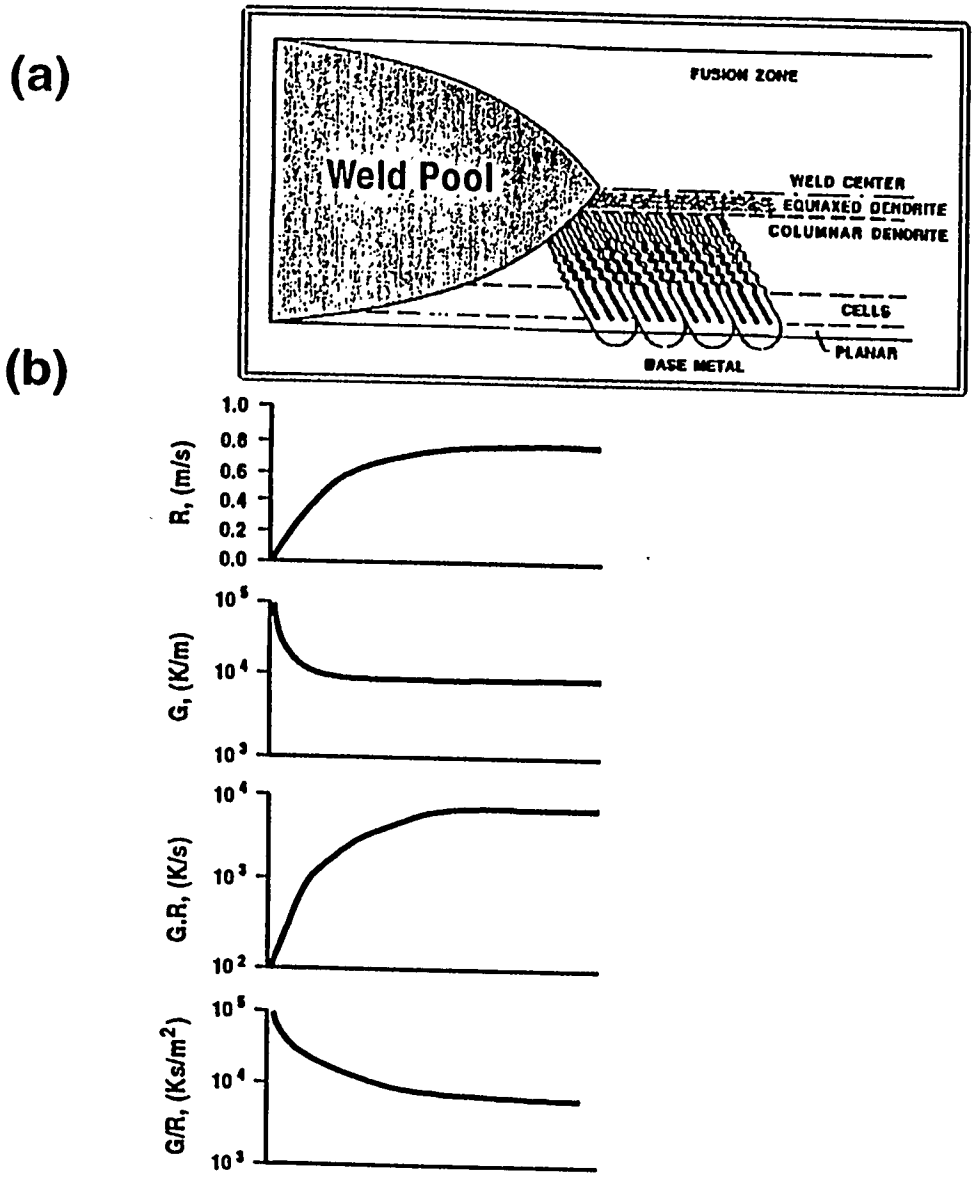


Fig. 9 (a) Schematic illustration of weld microstructure across the fusion zone and (b) corresponding schematic variation of G, R, GR and G/R values as a function of position.

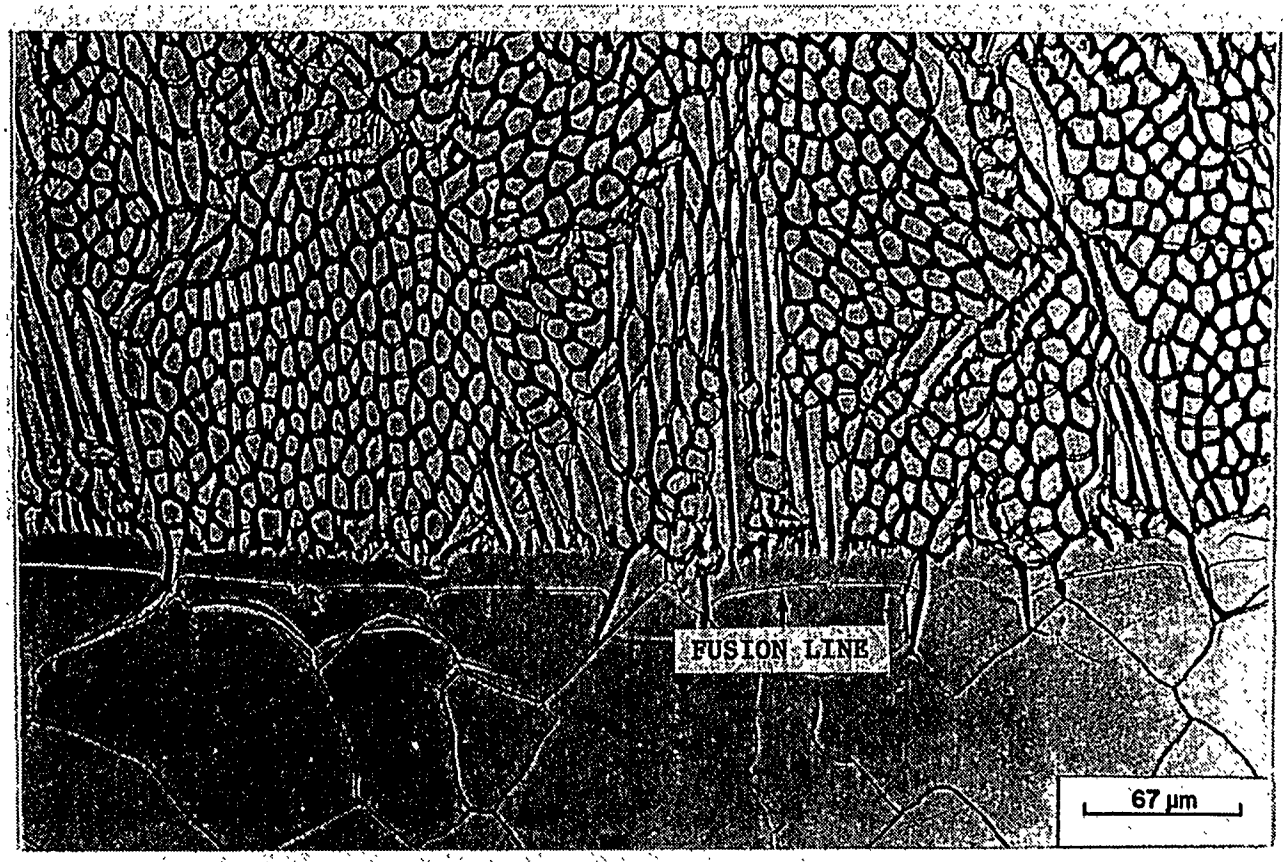


Fig. 10 Optical micrograph of stainless steel weld metal region and heat affected zone. The micrograph clearly shows the fusion line, with planar growth; region of transition from planar to cellular growth; and the region of cellular growth.

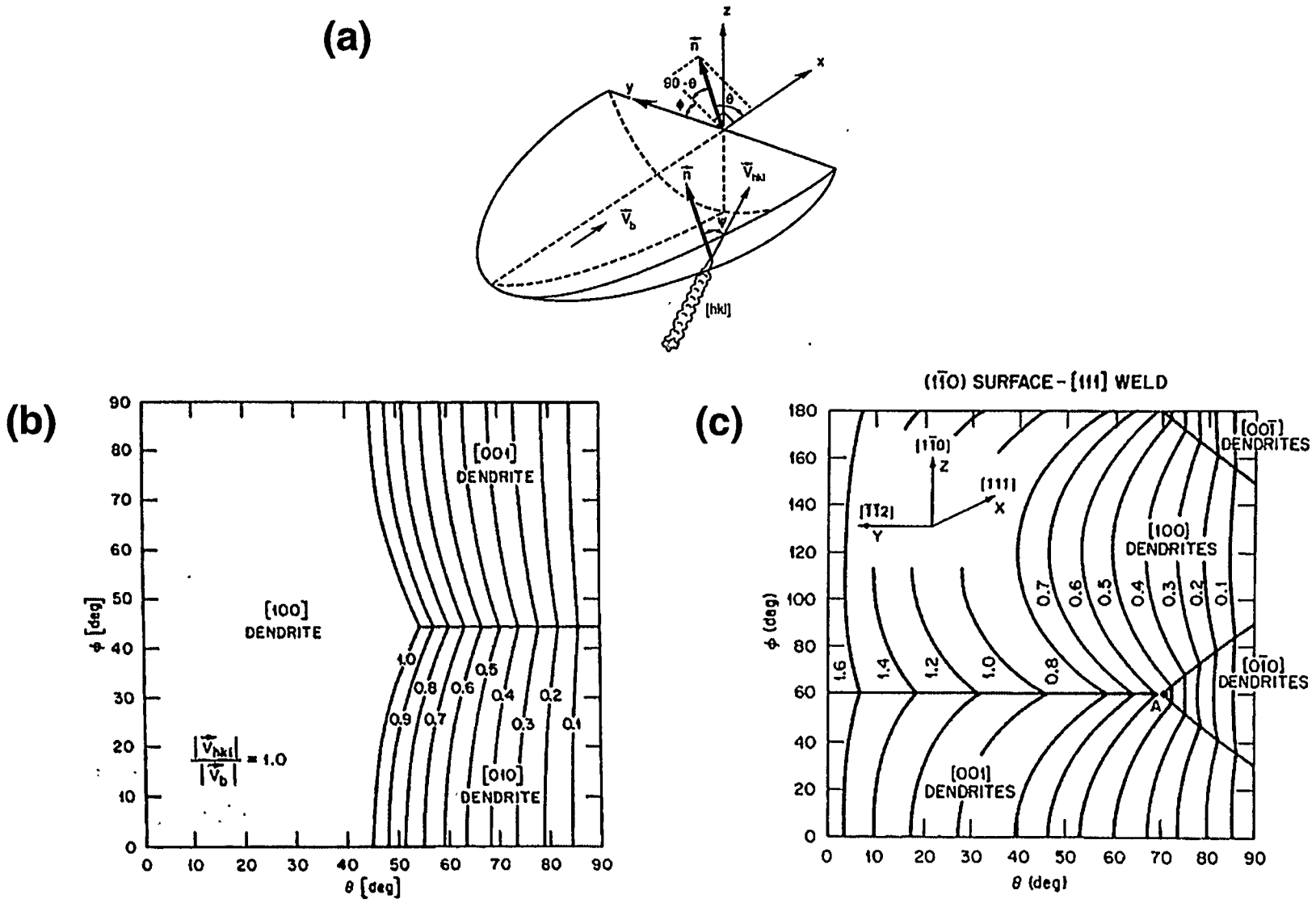


Fig. 11 (*a*) Schematic diagram of the weld pool showing the orientation of the fixed set of reference axes, *x*–*y*–*z*, and the angles ψ, ϕ, and θ (the *z*–axis of this reference frame is perpendicular to the top surface of the bicrystal, and the *x*–axis coincides with the welding direction); (*b*) velocity isopleth map of the minimum dendrite tip velocity $|V_{hkl}|$, normalized to the beam velocity $|V_b|$, as a function of the orientation angles θ and ϕ of the solidification front normal $n$ for a weld in the [100] direction on (001) face of the crystal; and (*c*) for a weld in the [111] direction on (1$\bar{1}$ 0) face of the crystal.

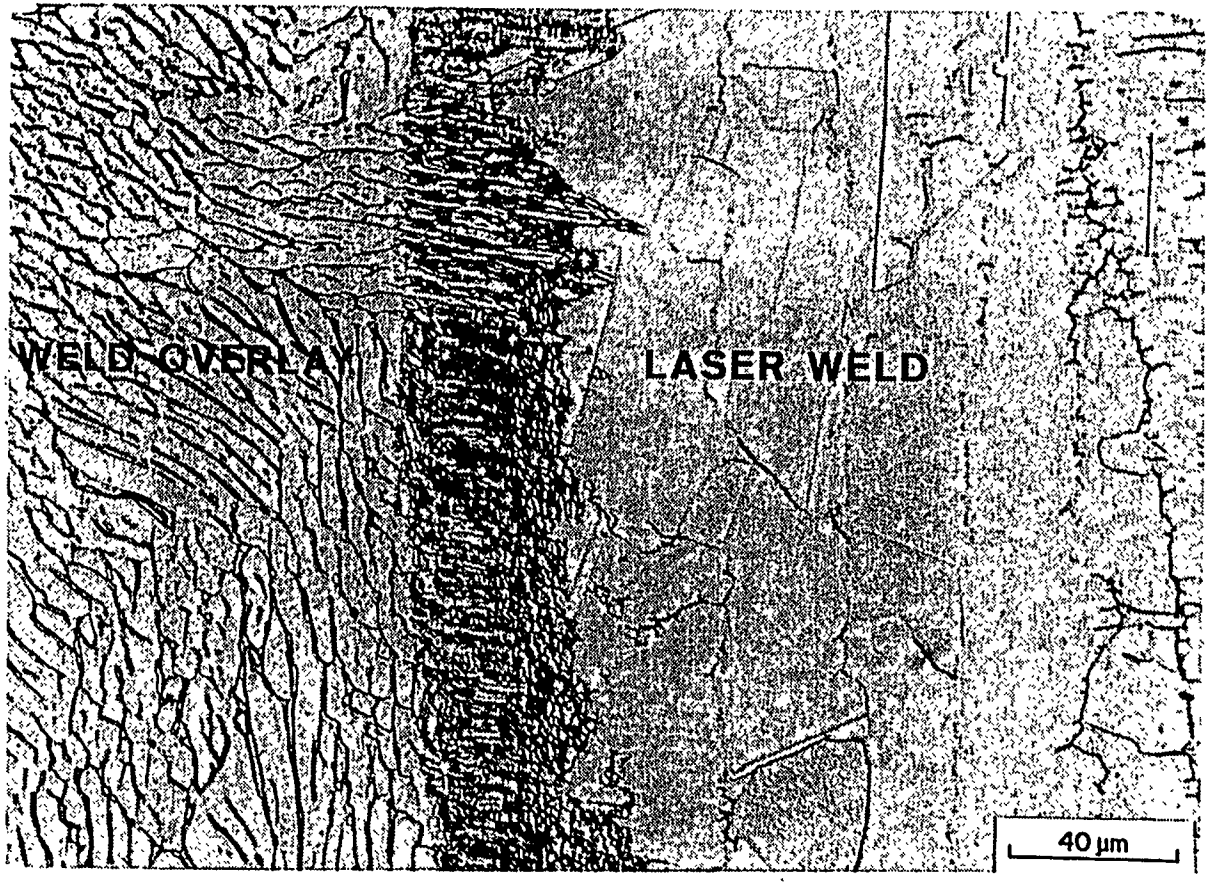


**Fig. 12 Duplex (austenitic plus ferrite) structure in conventional weld overlay and fully austenitic structure obtained by autogeneous laser weld on the same overlay.**

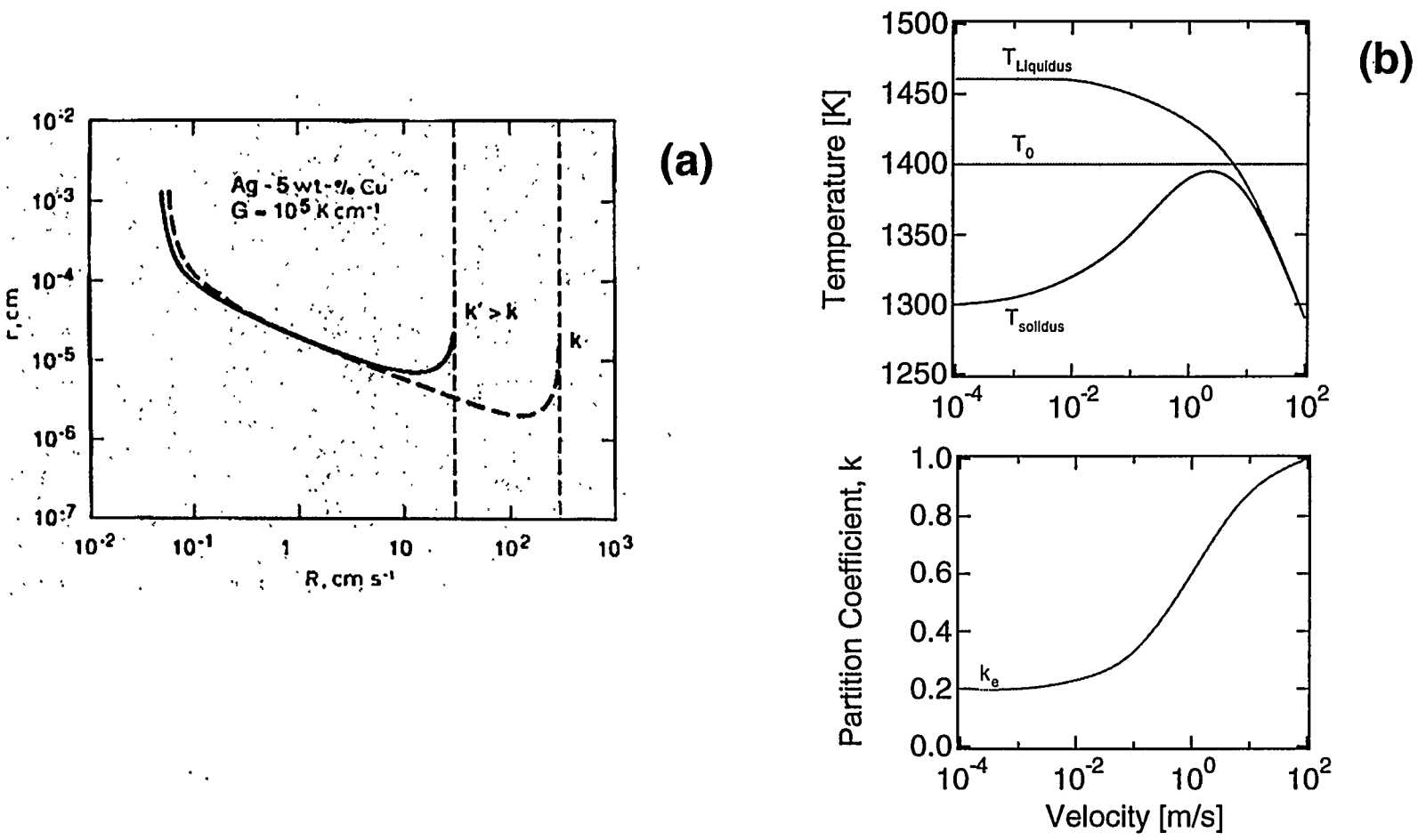


Fig. 13 (*a*) Effect of velocity–dependent partition coefficient on dependence of dendrite tip radius on growth velocity and (*b*) variation of nonequilibrium solidus and liquidus temperatures and partition coefficient as a function of growth velocity.[70]

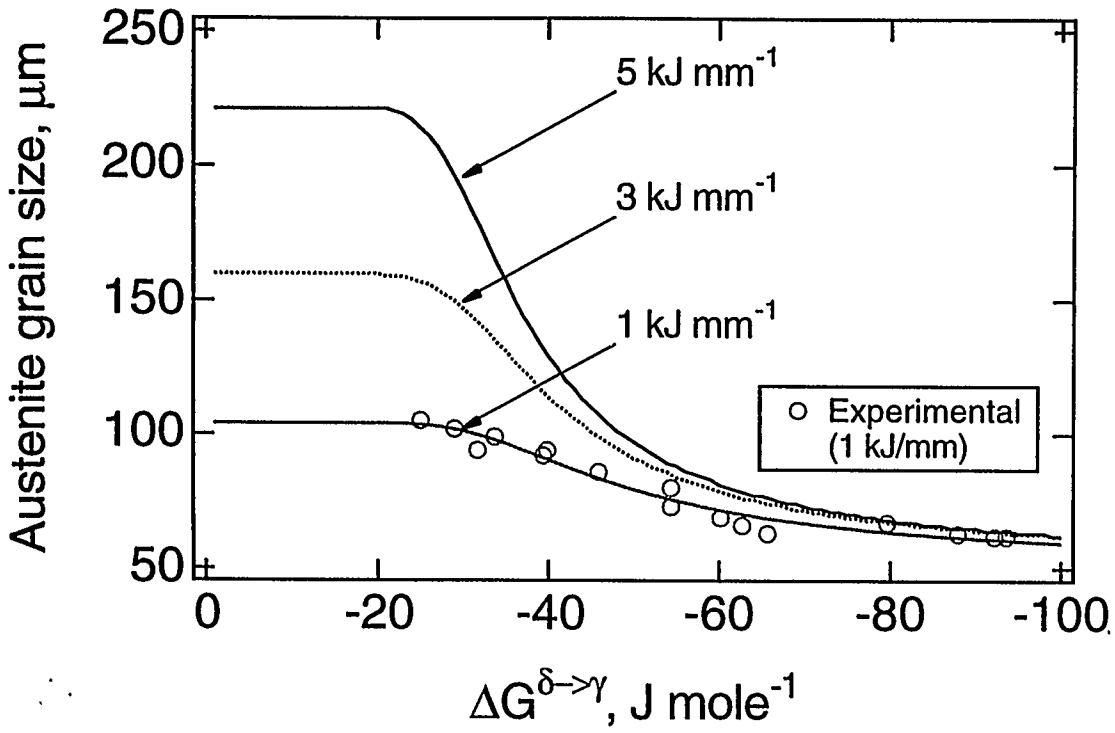


Fig. 14 The variation of austenite grain size (measured in welds deposited with a heat input of 1 kJ $mm^{-1}$) with driving force for transformation of δ ferrite to austenite ($\Delta G^{\delta\rightarrow\gamma}$). The dark line is the fitted line with a relation given by Eqs. (4) and (5). Experimental data (open circles) are from ref. 83. The curves for 3 and 5 kJ $mm^{-1}$ are drawn schematically to illustrate the expected variation.

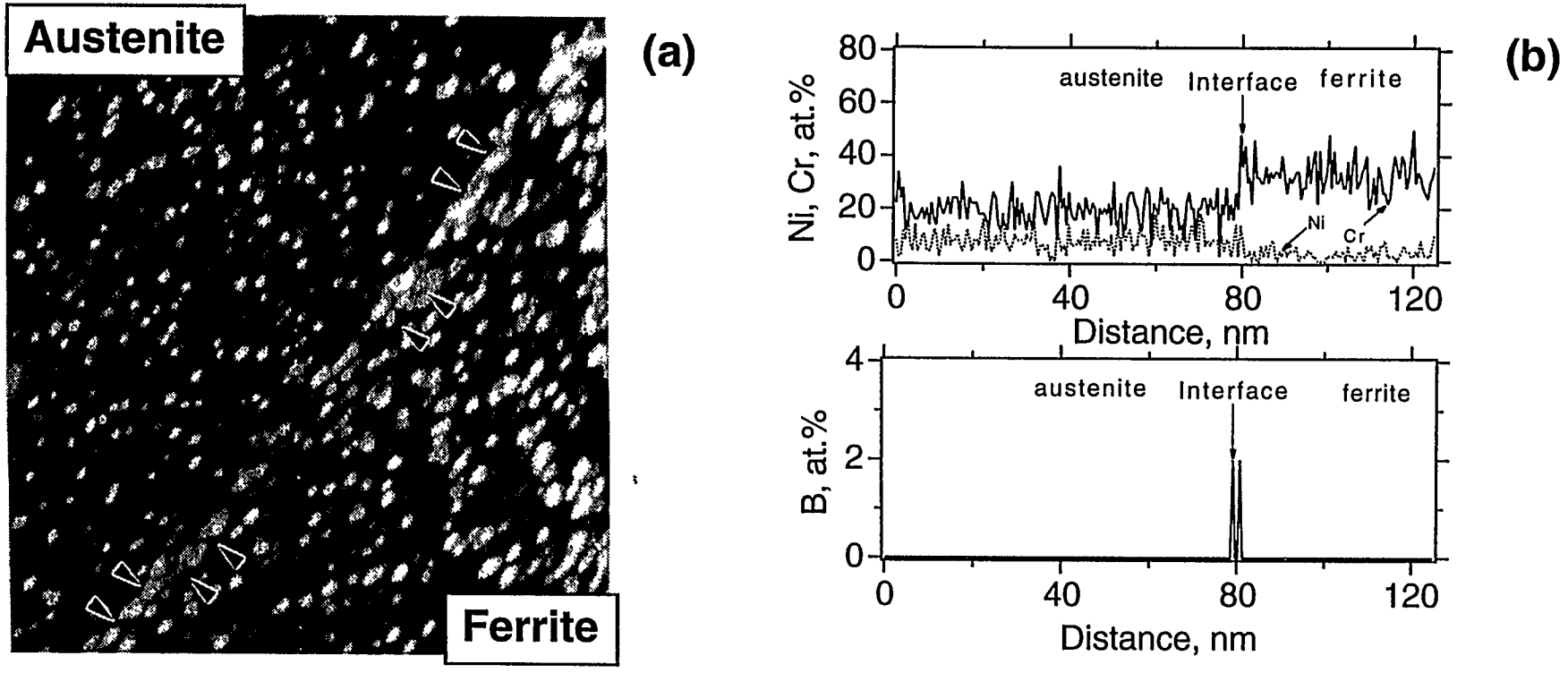


Fig. 15 (*a*) Field ion micrograph of the as-welded sample showing (δ) ferrite–austenite boundary and (*b*) composition profile indicating the presence of boron along the (δ) ferrite–austenite boundary.

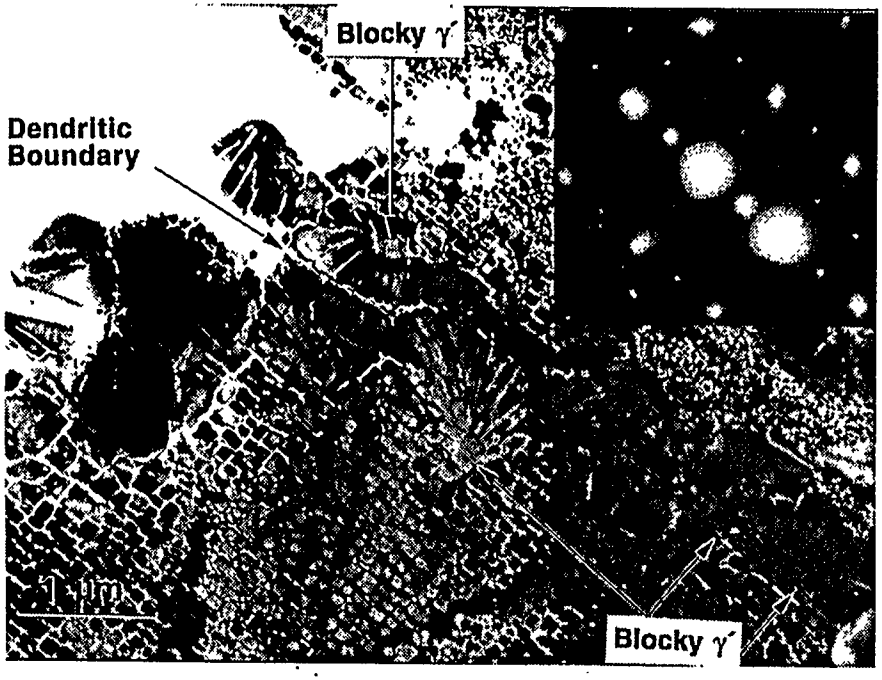


(a)

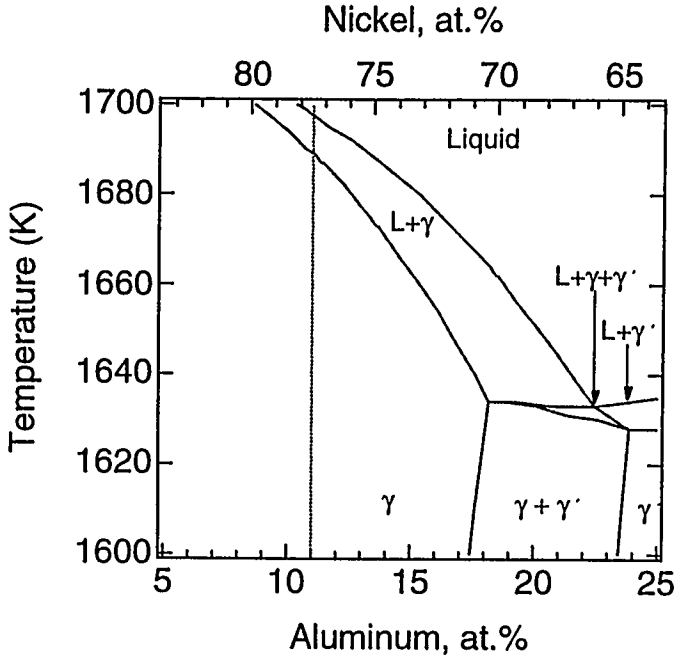


(b)

Fig. 16 (*a*) Transmission electron micrograph of the PWA-1480 weld metal region in the as-welded condition showing two dendritic grains, dendritic boundary, and eutectic $\gamma'$ precipitate (marked by an arrow) along the dendritic boundary. The electron diffraction pattern (inset), taken near to the $[001]_\gamma$ zone, shows the superlattice reflections from $\gamma'$ precipitates. (*b*) A quasi-binary diagram of the Ni-Al-Cr system with 11.5 at. % Cr calculated by ThermoCalc™ software.[25] The dotted line shows the composition corresponding to 11.0 at. % Al. In this phase diagram, the tie lines are not in the plane of the diagram.